MARK, NICHOLAS R., M.S. A New Crossed Molecular Beam Apparatus for the Study of the Cl + O_3 Reaction Probed Via Direct Absorption of Millimeter/Submillimeter-Waves. (2012)
Directed by Dr. Liam M. Duffy. 87 pp.

For decades, molecular beam scattering experiments have been used to understand the forces and dynamics that are involved in chemical reactions at the quantum mechanical level. Using millimeter/submillimeter-waves the dynamics for the scattering of a bimolecular collision can be probed via pure rotational spectroscopy. Focus of this research is the reaction between ozone and chlorine, which has been widely studied due its key role in the catalytic destruction cycle of ozone in the atmosphere.

For this research, a new crossed molecular beam apparatus was successfully designed and constructed. The apparatus consists of independently rotating arms to allow for reactants to be collided at a wide range of angles, and therefore relative velocities, and can easily be adapted for use in numerous types of scattering experiments. Ozone was successfully created and trapped to produce a molecular beam, which has been characterized from a pinhole and slit nozzle. Though no products have been seen from the experiments to date, the critical work has been completed so the system can be optimized in the future.

A NEW CROSSED MOLECULAR BEAM APPARATUS FOR THE STUDY OF THE $Cl + O_3$ REACTION PROBED VIA DIRECT ABSORPTION OF MILLIMETER/SUBMILLIMETER-WAVES

by

Nicholas R. Mark

A Thesis Submitted to
The Faculty of the Graduate School at
The University of North Carolina at Greensboro
in Partial Fulfillment
of the Requirements for the Degree
Master of Science

Greensboro
2012

Approved by

_____
Committee Chair

APPROVAL PAGE

This thesis has been approved by the following committee of the Faculty of the Graduate School at the University of North Carolina at Greensboro.

Committee Chair_____

Committee Members _____

_____

_____
Date of Acceptance by Committee

_____
Date of Final Oral Examination

ACKNOWLEDGEMENTS

I would like to thank my faculty mentor, Dr. Liam Duffy, for his time, commitment, and guidance toward my research and in the preparation of this thesis. I also would like to thank my research committee members, Dr. Alice Haddy and Dr. Bruce Banks. Also, I would like to express my appreciation to the entire faculty and staff of the Chemistry and Biochemistry Department at UNCG.

Finally, I would like to thank my family and friends for all their support throughout my academic career and life.

TABLE OF CONTENTS

Page

LIST OF FIGURES

Page

CHAPTER I

BACKGROUND

I.A Introduction

Gas-phase molecular reaction dynamics has existed for decades, with the goal of understanding chemical change at the atomic and quantum mechanical level. Examining reactions at this level via molecular beam scattering has provided numerous advances on the comprehension of chemical physics and the intermolecular forces that are involved in chemical reactions [1-8], which has, in time provided insight into more macroscopic fields such as atmospheric chemistry, astrochemistry and plasmas. By controlling the energies and orientations of the reactants in a scattering experiment, the electronic and nuclear motions of molecules and how they are coupled in elastic and reactive collisions can be investigated.

Crossed molecular beam experiments usually consist of two molecular beam sources that are oriented 90° to one another, which can be seen in Figure 1.

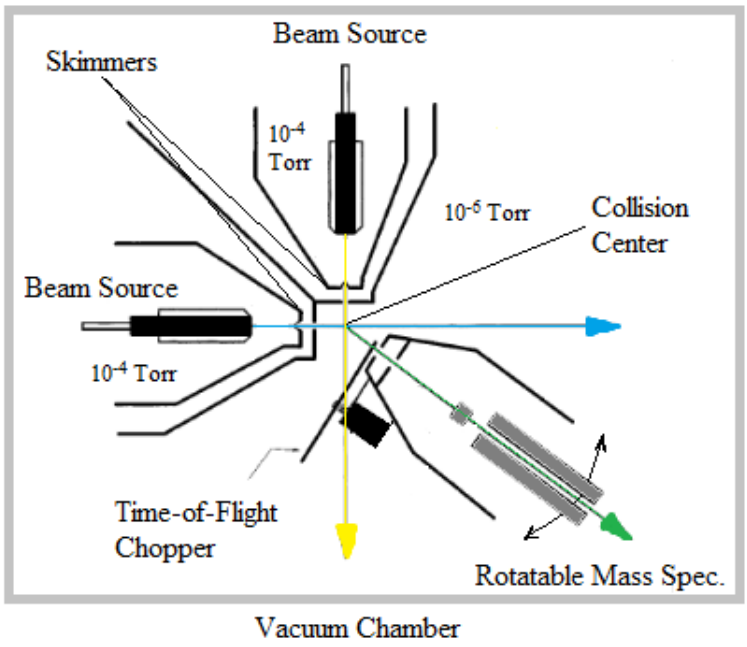

Figure 1. Schematic of the "universal" crossed molecular beam apparatus. Molecular beams are crossed at 90° in a vacuum chamber and detected using a rotatable mass spectrometer.

Historically, the crossed molecular beam apparatus shown above is typically regarded as the "universal" setup. By using a rotatable time-of-flight mass spectrometer, both the time and angle measurements of a chemical reaction can be elucidated. These measurements yield trajectories and the translational energy release of the product molecules under single collision conditions, allowing for accurate angular and velocity distributions to be found [1]. The experimental distributions can then be compared to theoretical predictions, i.e. intermolecular and potential energy surfaces, to understand how chemical reactions proceed.

A supersonic molecular beam is produced when high pressure gas is forced through a small, approximately 100 µm, nozzle into a differentially pumped chamber and then typically collimated downstream using a skimmer. As the parent gas molecules pass through the nozzle from a high pressure environment into vacuum conditions, they experience an adiabatic supersonic free jet expansion. This expansion leads to a cold, supersonic, usually 500-1000 m/s, beam of molecules that are directed away from the nozzle aperture [3-4].

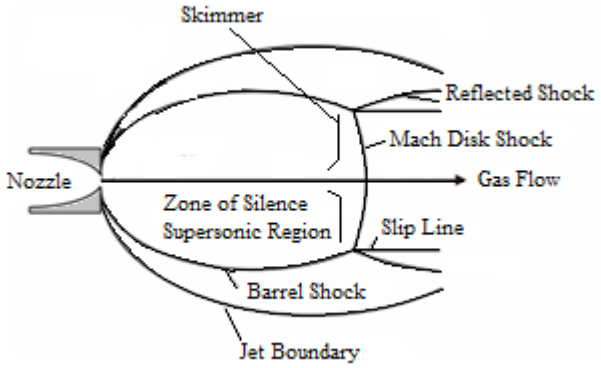

Figure 2. Diagram of supersonic free jet expansion. Static gas at high pressure located in the nozzle, is expanded through the nozzle into a vacuum chamber. Upon exiting from the nozzle the gas undergoes adiabatic expansion and becomes supersonic, in the zone of silence region. To limit the divergent parts of the free jet and their background with the mass spectrometer, skimmers are typically placed within the zone of silence region, yielding a narrow supersonic beam after the skimmer.

I. B Molecular Scattering

I. B.1 Hard Spheres

The typical crossed molecular beam experiment involves bimolecular, single collision conditions. These collisions can result in elastic scattering, inelastic scattering or reactive scattering. Elastic scattering involves the conservation of kinetic energy of the species in the center-of-mass frame and only the flight path of colliding species is altered. Inelastic scattering is a process that results in the kinetic energy of an incident particle not being conserved, i.e. there a loss or gain of energy. Both inelastic and elastic scattering do not involve a change in the chemical composition of the reactants; when this occurs it is considered reactive scattering. To undergo a chemical reaction the molecules must get close enough to experience a change in energy, mass or charge. In reality the interactions between the two molecules can become very complicated, when trying to look at each individual atom and its electrons. The molecular orbitals, interaction potentials and hence dynamic forces of the molecules will determine if a chemical reaction will occur.

A crude way to model a two body collision is to consider the molecules as simple hard spheres, as depicted in Figure 3 [6]. When the hard spheres are at a distance greater than their diameters they do not interact, however once the distance between the spheres decreases to the length of d the hard spheres will repel one another. The value of d is given simply as the sum of the radii of the two individual hard spheres and in turn can be used to define an area of exclusion or collisional cross section, $\sigma = \pi d^2$, as indicated by the dashed circle in Figure 3.

The size of d for any hard sphere collision is dependent upon the electrostatic forces between the colliding species. For example, if two polar molecules were to collide then there would be some sort of attractive and repulsive forces that will determine the value of d depending on the orientation of the molecules. Thus, each pair of colliding molecules will have a different value for d. So that in the crude picture of colliding hard spheres, d and hence σ can be thought of as effective average diameters and cross sections for the scattering phenomena.

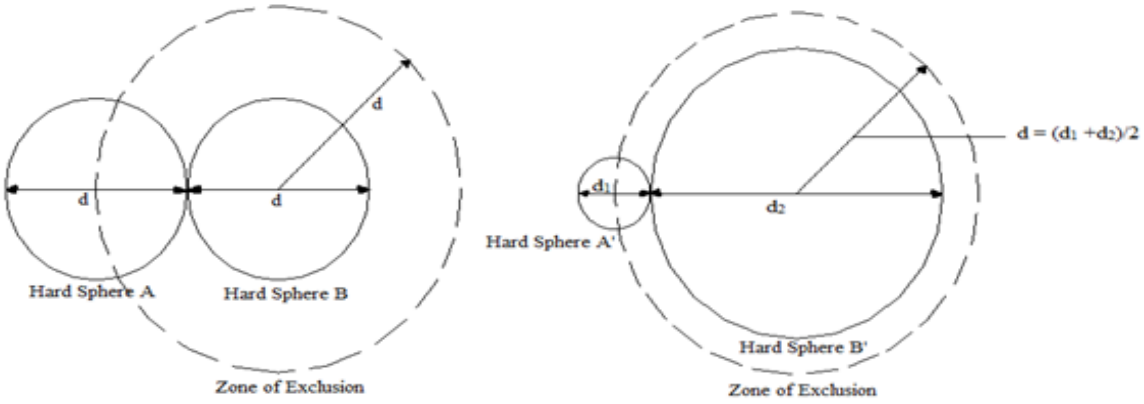

Figure 3. Collision cross section of hard spheres. Left: Collision cross section of equal sized hard spheres. Area of exclusion has a radius of d. Right: Collision cross section of unequal spheres. Area of exclusion radius is the sum of the radii of the two hard spheres or $(d_1 + d_2)/2$ [6].

Conceptually, the easiest way to view two body collisions is in the inertial frame of reference where one of the reactants is placed at the center and the other approaches it along a straight line. As the reactants approach one another, there will be an interaction that may result in some form of chemical transformation or deflection. Typically the interaction between two molecules is attractive at long range and highly repulsive at short

range. If the interaction was purely repulsive the scattering event could be approximated using the hard spheres model. For hard spheres, the angle at which the two bodies deflect, χ, is given as [6]:

$$\chi = 2\arccos(b/d) \tag{1.1}$$

It is dependent upon the "impact parameter," b, which is the perpendicular distance between the colliding species, depicted in Figure 4, and d, the hard sphere range of repulsion [6]. For instance, if b > d, then there would be no scattering of the two hard spheres, they would simply pass by one another without interaction and therefore $\chi = 0$ [6]. Also, when b = d the two hard spheres will simply just graze one another and there will be no deflection.

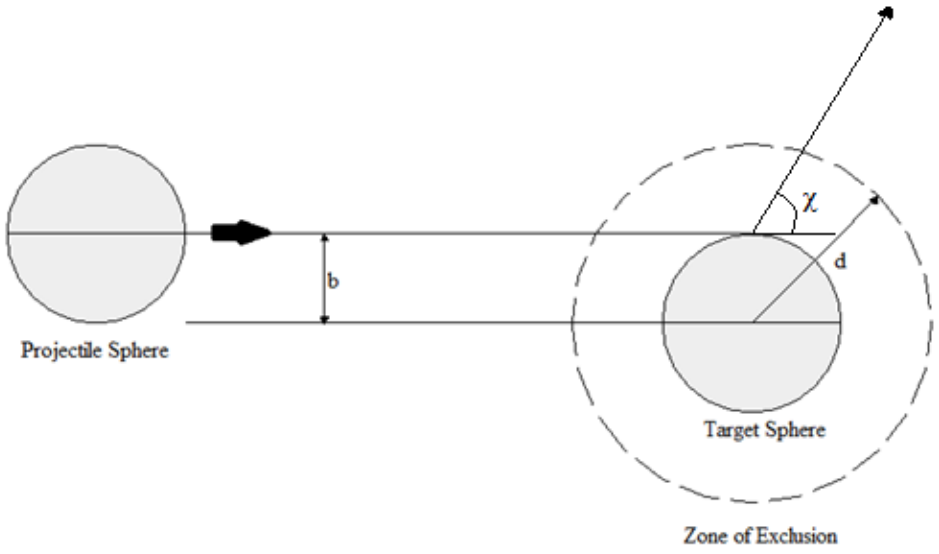

Figure 4. Diagram of the trajectory for a hard sphere collision. The impact parameter, b, is the perpendicular distance between the center of the two hard spheres. The deflection angle χ is dependent upon the impact parameter and range of the zone of exclusion. When the impact parameter is greater than d, there will be no deflection.

I.B.2 Elastic Scattering

For real non-hard sphere collisions, the deflection angle function $\chi(b)$ depends on the shape of the intermolecular potential, e.g. Lennard-Jones Potential seen in Figure 5.

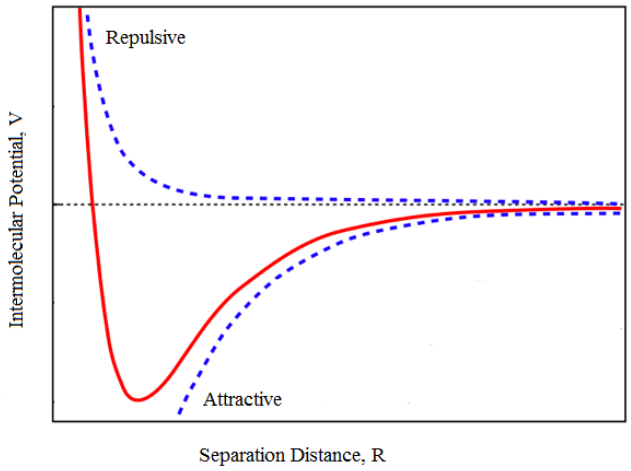

Figure 5. Lennard-Jones potential. The Lennard-Jones potential represents the intermolecular potential between two atoms or molecules. At long separation distances the attractive force predominates, while at shorter distances the repulsive force is steeply dominate. The depth of the potential well correlates to a strength of interaction between the particles.

Figure 6 shows a distribution of collision trajectories for various values of the impact parameter and the resulting deflection angles for elastic scattering at a single collision energy.

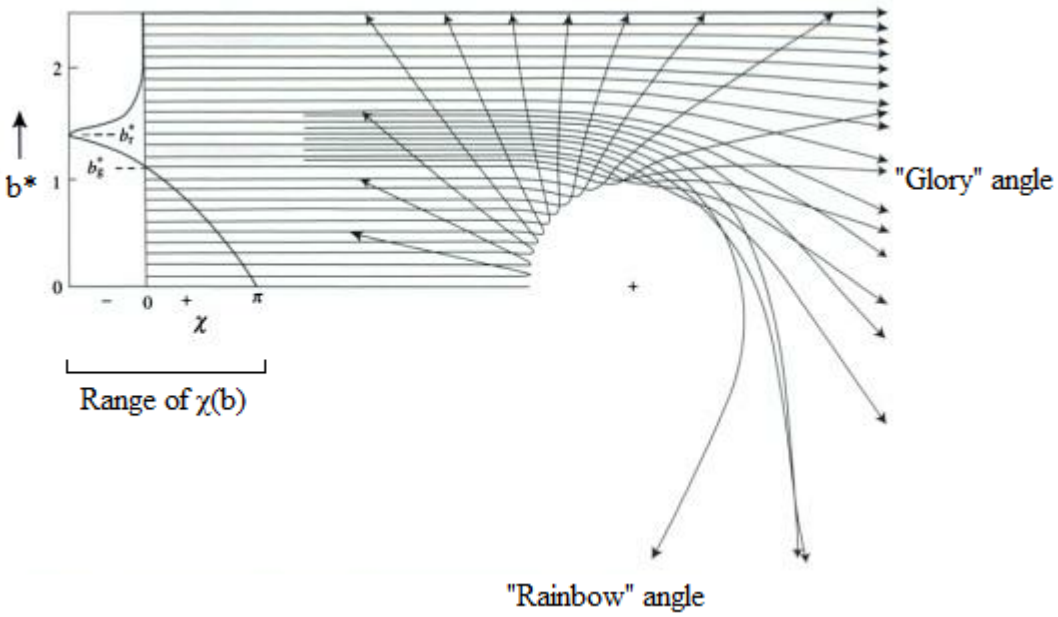

Figure 6. Elastic scattering of a two body collision. Collision trajectories represented by the lines as one body approaches the center body. The y-coordinate is $b^* = b/R_m$, the reduced impact parameter, where R_m is the equilibrium distance of the well in the potential. The "rainbow" angle, b_r, is the trajectory with the largest negative χ and the "glory" impact parameter, b_g, results in $\chi = 0$ [adapted and reprinted with the permission of Cambridge University Press].

When the impact parameter is large, there is minimal to no interaction and only a slight long-range attractive force is felt by the molecules as seen in the trajectories deviating toward the center target and resulting in a small negative χ value as depicted in Figure 6. As the value of b continues to decrease, the influence of the repulsive force begins to play a role, and eventually the most negative value of χ is reached at b_r, also known as the "rainbow" angle [5,6]. At this "rainbow" angle the attractive and repulsive forces between the two bodies balance one another to result in a very large, almost orbiting deflection. The "rainbow" angle is where over the course of its trajectory the two molecules feel the largest integrated attractive force between one another and

depending on the collision energy, roughly corresponds to the bottom of the potential well.

Once the impact parameter has dropped below the "rainbow" angle, the value of χ begins to increase and the repulsive force becomes progressively important. Eventually the two molecules will come to a point where they experience an equal amount of integrated attractive and integrated repulsive forces that results in a deflection of $\chi = 0$ and the incident molecule will continue along its initial path of travel, this is called the "glory" impact parameter, b_g. [5,6]. After the "glory" impact parameter has been passed, the repulsive force between the molecules dominates. Eventually as b decreases to 0, the repulsive force eventually leads to the molecules not being able to approach any closer and the collisions become more head-on, resulting in backscattering of the molecules.

I.B.3 Reactive Scattering

Figure 6 depicts a collision event from the fixed point at the middle of one of the collision partners; however these same collisions may be followed in the laboratory or center-of-mass (c.o.m.) frames of reference. While the laboratory is the frame of reference of the molecular beams in the experimental setup, it is the c.o.m. or molecular frame of reference that is relevant to the understanding of molecular level interactions. The conversion from the laboratory to center-of-mass frame of reference can be done with a "Newton diagram," which depicts both the velocities before and after collision on a single diagram as seen in Figure 7, and provides a kinematic analysis of the reaction [6]. In this figure, the velocities in the laboratory frame are represented by $\mathbf{v}_1$ and $\mathbf{v}_2$

while the relative velocities in the center of mass frame are $\mathbf{u}_1$ and $\mathbf{u}_2$. The velocity of one of the products after the collision is represented by $\mathbf{u}_1$' and has an angle, θ, from the initial relative velocity in the c.o.m. system. When the collision occurs the ejected molecules will scatter in random directions, however they will have a fixed recoil energy and will be confined to scatter in an expanding sphere around the c.o.m. as seen in the Figure 7. The products will normally not be uniformly distributed over the surface of the sphere, depending on the nature of the chemical reaction and the orientation of the reactants. The measurement and mapping of these velocity distributions is the principal goal of any crossed beam experiment, yielding insight into the electronic states involved in the reaction.

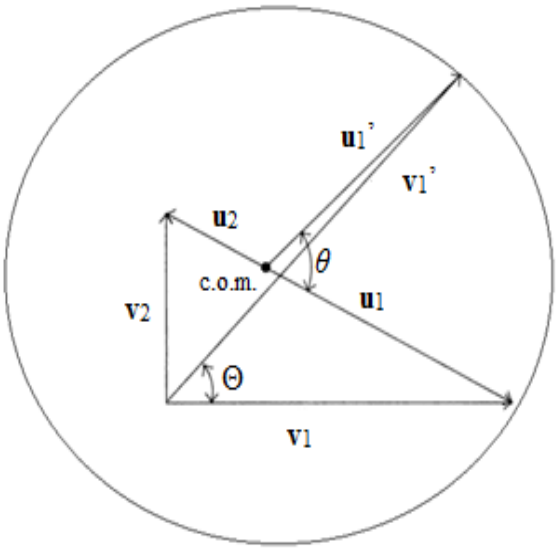

Figure 7. Newton Diagram for generic reaction. The laboratory frame is denoted by v and the center-of-mass frame is denoted by u. The θ is the angle of scattering in the center-of-mass frame and Θ is the angle between the initial and final laboratory velocities. v_1' is the product or elastic/inelastically scattered parent molecule.

The possible array of velocity vectors after a two body collision can be further separated into a discrete set of "Newton spheres," which correspond to the partitioning of the total energy based on the translational and internal states of the reaction. Conservation of total energy gives the following equation [6]:

$$E_{tot} = E'_{int} + E'_{trans} = E_{int} + E_{trans} - \Delta E_0 \qquad (1.2)$$

In this equation, ΔE_0 is a known standard reaction energy change for a given reaction. By the conservation of energy, the quantum ro-vibrational states, E'_{int}, that are accessible and final velocities of the collision products, E'_{trans}, are dependent upon the initial relative

translational energy in the c.o.m. frame, E_{trans}, and the initial internal energy of the reactants, E_{int}.

Figure 8 shows a potential energy profile where the concentric spheres have radii that correspond to the different vibrational states of the products. Within each of these vibrational state manifolds are contour plates, which correspond to the intensity distribution of various accessible rotational and translational states of the products [6]. From these distributions, information about the potential energy surfaces of the reaction can be revealed, such as its shape, if the reaction has a barrier to overcome or the possibility of intermediate complexes formed during scattering.

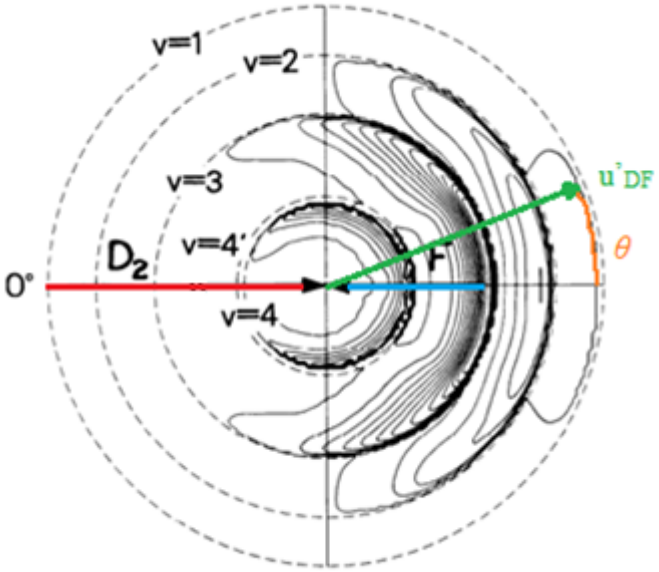

Figure 8. Newton Spheres for the D_2 + F reaction. Each sphere is a vibrational state accessible to the reaction product DF while the contours between correspond to various distributions of rotational and translation states [adapted and reprinted with permission © The Nobel Foundation, from Y. T. Lee's Nobel Lecture].

I.C O_3 + Cl

I.C.1 Catalytic Ozone Destruction Cycle

The catalytic ozone destruction cycle has been an important topic in atmospheric chemistry due to its being the primary reason for the creation of the ozone holes in the polar regions, as well as the thinning of the ozone layer in the mid-latitude region. One of main reactions in the catalytic cycle and the focus of this study is:

$$Cl + O_3 \rightarrow ClO + O_2$$

There are similar reactions with the other halogen atoms (F, Br) and ozone, which form molecular oxygen and halogen oxides.

The source of the halogen atoms in the atmosphere has been attributed to man-made halocarbon refrigerants, which the international community has been phasing out based on the international treaty known as the Montreal Protocol. These chlorofluorocarbons are photodissociated in the atmosphere to form the halogen atoms, and are the basis for the two catalytic cycles that attribute to most of the ozone loss in the polar regions of the stratosphere:

(I) ClO dimer mechanism: [10]

$$2(Cl + O_3 \rightarrow ClO + O_2)$$

$$2ClO + M \rightarrow (ClO)_2$$

$$(ClO)_2 + h\nu \rightarrow Cl + ClOO$$

$$ClOO + M \rightarrow Cl + O_2 + M$$

$$\text{net:} \quad 2O_3 \rightarrow 3O_2$$

(where M is any air molecule)

(II) ClO/BrO mechanism: [11]

$$Cl + O_3 \rightarrow ClO + O_2$$

$$Br + O_3 \rightarrow BrO + O_2$$

$$ClO + BrO \rightarrow Cl + Br + O_2$$

$$\text{net:} \quad 2O_3 \rightarrow 3O_2$$

I.C.2 Prior Ozone-Halogen Studies

Due to the large environmental importance of the ozone layer in absorbing nearly 97-99% of harmful UV radiation, there have been numerous studies on the kinetics and dynamics of the Cl + O_3 radical reaction and other reactions following the X + O_3 (X = O(^{3}P), F, Cl, Br) form [9, 12-22]. Kinetic studies have determined that the X + O_3 reactions, with the exception of H + O_3, have pre-exponential values in the Arrhenius equation, $k = Ae^{-E_a/RT}$ consistently around 2.2 x 10^{-11} cm^3 molecule^{-1} s^{-1} [12-18]. In comparison, if every collision resulted in a reaction the pre-exponential value would be ~1.7 x 10^{-10} cm^3 molecule^{-1} s^{-1}, so approximately 1 in 10 collisions results in a reaction.

This fairly high pre-exponential factor is indicative of a large reactive cross section, which will allow the formation of large product number densities giving the best chance of reaction and hence signal in this crossed molecular beam study. When diatomic radicals, e. g. NO, OH or SO, were reacted with ozone the pre-exponential factor dropped by a factor of ten to 2.2 x 10^{-12} cm^3 molecule^{-1} s^{-1} [16-18]. This order of magnitude difference in pre-exponential factors can likely be attributed to the orientation of the diatomic radicals during a collision. For example, if the diatomic radical, OH, was to collide with an ozone molecule, the orientation of the radical in regard to ozone could result in there being a reaction or simply a collision.

One interesting note from the kinetics studies is that the rate coefficients were insensitive to the reaction exothermicity, instead the electron affinities of the radical species dictated these values [16-18]. Based on this, it was hypothesized that the

transition state structures largely resembled ozone and the reactions likely preceded through an early transition state [14-15].

Later studies on the $Cl + O_3$ reaction, including numerous theoretical [21-22,25-27], crossed molecular beam time-of-flight [9], matrix spectroscopy [23] and laser induced fluorescence in both gas cells and under vacuum [19-20,24], proved that the reaction did proceed through an early transition state. This early transition consists of the chlorine radical approaching one of the terminal O-O bonds on the ozone, which possibly forms a very short lived unstable ClO_3 intermediate, which can be seen in Figure 9. This co-planar asymmetric attack of the terminal oxygen seems to be the only feasible way for the chlorine radical to abstract an oxygen atom. The other possible interaction would be if the chlorine radical attacked perpendicular to the ozone plane, however this has not been observed [9, 19]. If this type of interaction occurred it would likely create a relatively stable and symmetric, D_{3h}, intermediate as shown in Figure 8, however there is a high energy barrier than would need to be overcome to create the intermediate leading to the unlikelihood of forming [19].

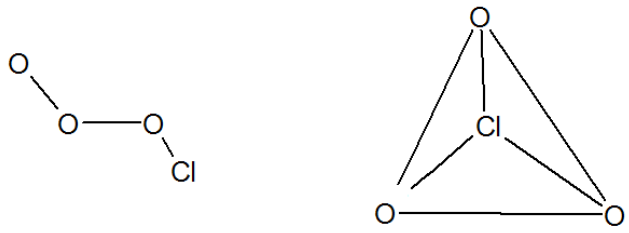

Figure 9. Possible intermediate species for O_3 + Cl reaction. Left: Co-planar attack of ozone, leads to very short lived intermediate and then abstraction. Right: Perpendicular attack, leads to stable/symmetric intermediate.

I.C.3 Product State Distributions

Typically the O_3 + Cl proceeds to form O_2 in the electronic ground triplet state, $^3\Sigma_g^-$. It is energetically possible to form the excited singlet state O_2, in either $^1\Sigma_g^+$ or $^1\Delta_g$ [9], as seen in Figure 10. However, these excited states have not been seen in any bulk thermal experiments to date [28-29]. In an experiment by Vanderzanden and Birks, a flow tube was used to detect O atoms from a secondary reaction. This secondary reaction involves an excited state $O_2(^1\Sigma_g^+)$ molecule produced from the initial Cl + O_3, reacting with another O_3 to form two ground state $O_2(^3\Sigma_g^-)$ molecules and a single O atom, $O_2(^1\Sigma_g^+) + O_3 \rightarrow 2O_2(^3\Sigma_g^-) + O$ [28]. Another experiment by Choo and Leu used a flow discharge/chemiluminescence detection method to try and detect either of the excited oxygen molecule products, $O_2(^1\Sigma_g^+)$ or $O_2(^1\Delta_g)$ [29]. Both studies showed that the formation of any electronically excited O_2 molecules was minimal. The ClO products have been found to form in the electronic ground $^2\Pi$ state. The first excited $A^2\Pi_\Omega$ state of ClO (311 kJ mol^{-1}, 74.3 kcal mol^{-1}) cannot be formed in the O_3 + Cl reaction because the

exothermicity of the reaction ($\Delta_R H$ = -162.6 kJ mol^{-1}, -38.8 kcal mol^{-1}) is insufficient [19].

ClO products have been found to have a vibrational state distribution with a maximum probability of the v = 4 state occurring. Although there has been inconsistency in this maximum value from other theoretical and experimental studies [19], such a vibrational population inversion is consistent with an early transition state. One of the goals of the research herein is to more fully characterize this vibrational distribution and augment it with rotational and hyperfine detail.

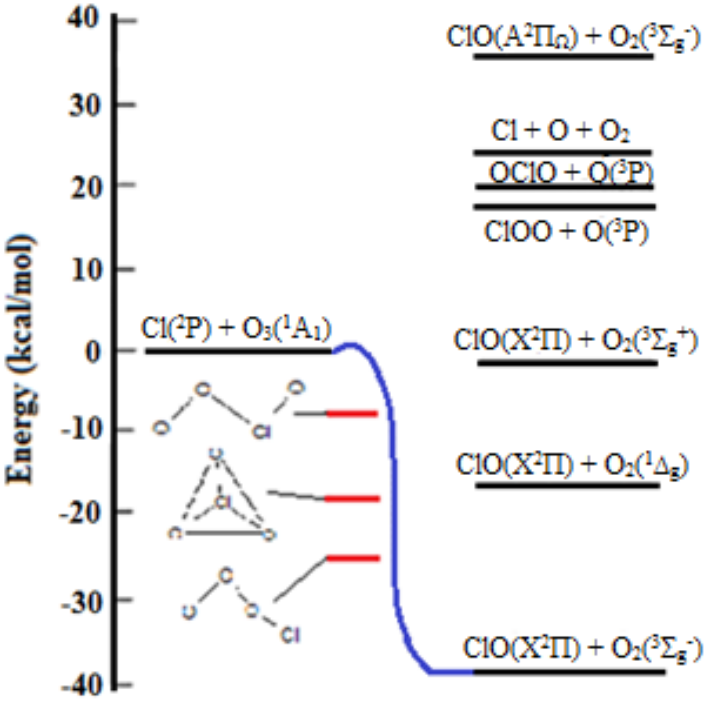

Figure 10. Energy level diagram for the O_3 + Cl system. The reaction proceeds through one of the three chlorine trioxide intermediates to the ground state products. The blue line represents the reaction pathway of the system. Activation energy is ~0.5 kcal/mol. Thermodynamic data is derived from [9, 18, 26-27].

I.C.4 Crossed Molecular Beam vs. Other Techniques

Though crossed molecular beam time-of-flight studies [9] may not be as state selective as techniques such as laser induced fluorescence (LIF) [19-20], which can be used for gas cell or molecular beam type experiments, techniques such as LIF have their own technical issues. LIF involves exciting the target species with a laser set to a specific wavelength and therefore a specific excitation, the excited molecule then will fluoresce, emitting a longer wavelength of light than the initial excitation, which can then be measured. In the Baumgartel et al. experiment, which involved the use of LIF in a gas flow cell, the main issue that arises is that only ClO transitions belonging to ($C^2\Sigma$ v' = 0,1) $\leftarrow$ ($^2\Pi$ v = 0-6) could be observed [19]. Also, for any of the transitions to v' = 1 during the fluorescence lifetime nearly 80% of the ClO will pre-dissociate before it is able to be measured [19]. Notably vibrational states as high as v = 20 have been shown to be energetically possible, but because of the pre-dissociation any vibrational state that was above v = 6 was not able to be measured using this technique without a large factor of uncertainty [19].

With this LIF experiment there was also a pump-probe delay of ~200 ns, and it was calculated that under these experimental conditions there would be ~2.4 gas kinetic collisions before a signal was measured [19]. The fact that there are multiple collisions makes it impossible to obtain Doppler profiles for a single collision reaction or measure the signal of real nascent products, which is one of the goals of the experiment described herein.

I.D Objectives

The objectives of the experiment are to design and build a new crossed molecular beam apparatus with independently rotating arms for the study of both inelastic and reactive scattering events. Another objective is to develop a system to create and trap ozone, to produce and characterize ozone in a molecular beam, as well as, create a discharge system for the creation of an atomic molecular beam of chlorine. The final objective is to use millimeter/submillimeter-wave technology to probe product state velocity and population distributions of nascent products and to determine differential scattering cross sections, as empirical evidence for theoretical predictions about the nature of the electronic states involved.

CHAPTER II

EXPERIMENTAL SETUP

The new crossed molecular beam apparatus featuring independently rotatable arms and probed via a pure rotational spectroscopy, along with other newly constructed devices for use in this study, will be described in detail later. A rendering of the setup can be seen in Figure 11.

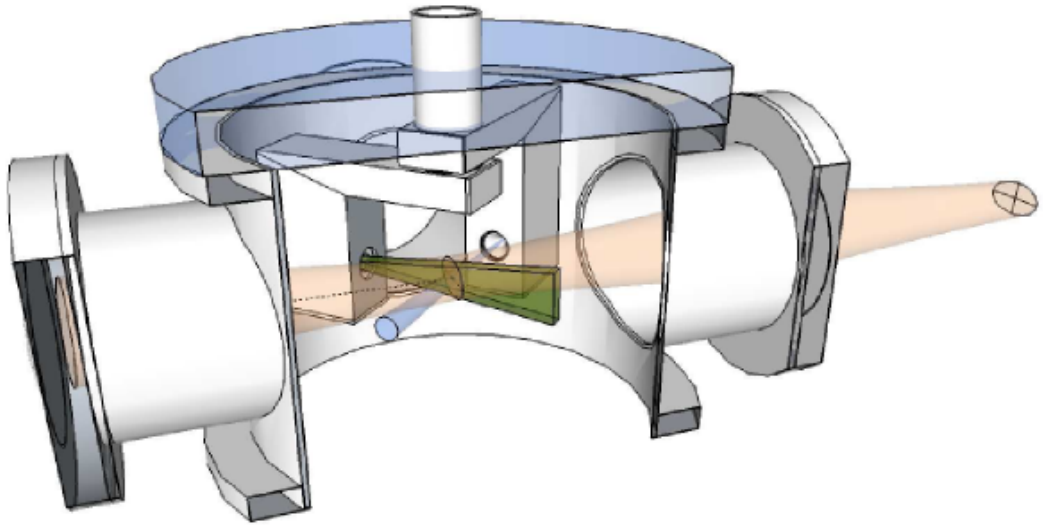

Figure 11. Cut-through view of crossed molecular beam chamber setup with independently rotatable arms.

Pulsed supersonic ozone and chlorine molecular beams were generated in a differentially pumped vacuum chamber arms and were crossed in the main collision chamber, which was typically at vacuum conditions of ~10^{-6} to 10^{-7} Torr.

II.A Molecular Beams

Ozone used in this experiment was generated using a commercially available ozone generator (Pacific Ozone, Model G11). The ozone is produced via corona discharge, where a pure oxygen stream is passed through a high voltage environment. This causes the breaking of the O_2 molecules and the subsequent formation of O_3. The ozone generator output was trapped on silica gel within a glass trap. The glass trap was cooled to approximately -78˚C using a dry ice/acetone bath [9,32-34]. The ozone generator was typically run for 20-30 minutes at 70% ozone production until enough of deep blue to purple ozone was absorbed on the silica gel. Once enough ozone was collected, the trap was removed incrementally from the chilled bath and argon was passed over the silica gel to form a gas mixture with the desorbing ozone, typical total stagnation pressures were between 600-700 Torr. To reduce the formation of ozone dimers and clusters, the nozzle was heated to 80˚C. When dealing with high concentrations of ozone, it was important to have a completely closed and cooled system. Because ozone is a strong oxidizer and hazardous at low concentrations, the generator and trap system was placed in a fume hood and the pressure inside the trap was kept below atmospheric pressure to reduce the possibility of leaks out to the laboratory. Any excess ozone not used in the experiments was carried via argon to a heated ozone steel pipe filled with

copper wire and exhausted into a laboratory hood. The ozone reacts with the copper to form CuO and O_2. At the end of the day, the trap system was well purged of any remaining gas.

The chlorine atomic beam was produced via electrical discharge of molecular chlorine (Specialty Gases of America). Stagnation pressures usually between 600-700 Torr were used, and the Cl_2 gas was used neat or seeded in helium and/or argon and then passed through a series of discharge plates, described in detail in results, with 500-700 V typically across them.

Both the ozone and chlorine molecular beams were produced using pulsed pinhole and slit nozzles, respectively (Parker Hannifin Corp., General Valve Division Series 99 and 97). The pinhole nozzle had an orifice size of ~300 μm and was tapered to produce a more intense molecular beam, while the slit nozzle had dimensions of 150 μm x 1.2 cm. The valves were controlled by a Parker's IOTA ONE Valve Driver, which was triggered by a pulse sequence from a Berkley Nucleonics Corp. Model 555 Pulse Generator, and consisted of the nozzle firing at a rate of 10 Hz, with the gas pulse width between 400-650 μsec long.

II.B Experimental Detection

The scattered products are detected using a direct absorption method involving linearly polarized microwave radiation, which is produced by commercially available millimeter/submillimeter-wave source modules from Agilent Technologies (Models 83557A and 83558A, which cover 50-75 GHz and 75-110 GHz respectively) that have

been nicknamed “armadillos” for their appearance [30]. The 75-110 GHz source modules were coupled with commercially available third party amplifiers (Spacek Labs Inc., Model SPW-18-14) and multipliers (Virginia Diodes Inc., Model VDI-WR5.1 x 2; 150-220 GHz or VDI-WR3.4 x 3; 225-330 GHz) to cover a wide range of frequencies with the exception of a small gap between 220-225 GHz. Using a microwave synthesizer (Agilent HP83623B) the source modules can be tuned to investigate rotational state specific collision products. These synthesizers can be operated in several different modes, i.e. continuous wave, modulated (AM or FM), swept, or pulsed, depending on the experiment [30].

When resonant microwave radiation is passed through polar molecules in the vacuum chamber, it is absorbed. The interaction between the radiation and molecules depends on the relative motion of the molecules with respect to the source. For example, a molecule that has no velocity component relative to the direction of the source will absorb at the prescribed “rest” frequency. While a molecule that is moving along the direction of the source, either away or towards, will experience a “shift” in the “rest” frequency, this is known as a Doppler shift. The difference in the power of the continuous mm/submm-waves, which were constantly hitting the detector, and the amount absorbed transiently by molecules in the reaction chamber was detected using a liquid helium cooled InSb hot electron bolometer chip made by QMC Instruments Ltd. (Model QFI/X). The bolometer was housed in a closed cycle cryostat developed by ColdEdge Technologies, consisted of the RDK-408D2 Cold Head, F-70L Helium Compressor and gas lines all from Sumitomo Cryogenics of America Inc. and a low

vibration interface designed by ColdEdge. The cryostat, which can be seen in Figure 12, was composed of two stages, 30 K and 4 K, which were connected to the low vibrational interface. The bolometer was connected to the low vibrational interface, and as liquid helium condenses heat was pulled from the bolometer to maintain a constant working temperature below 4.2 K.

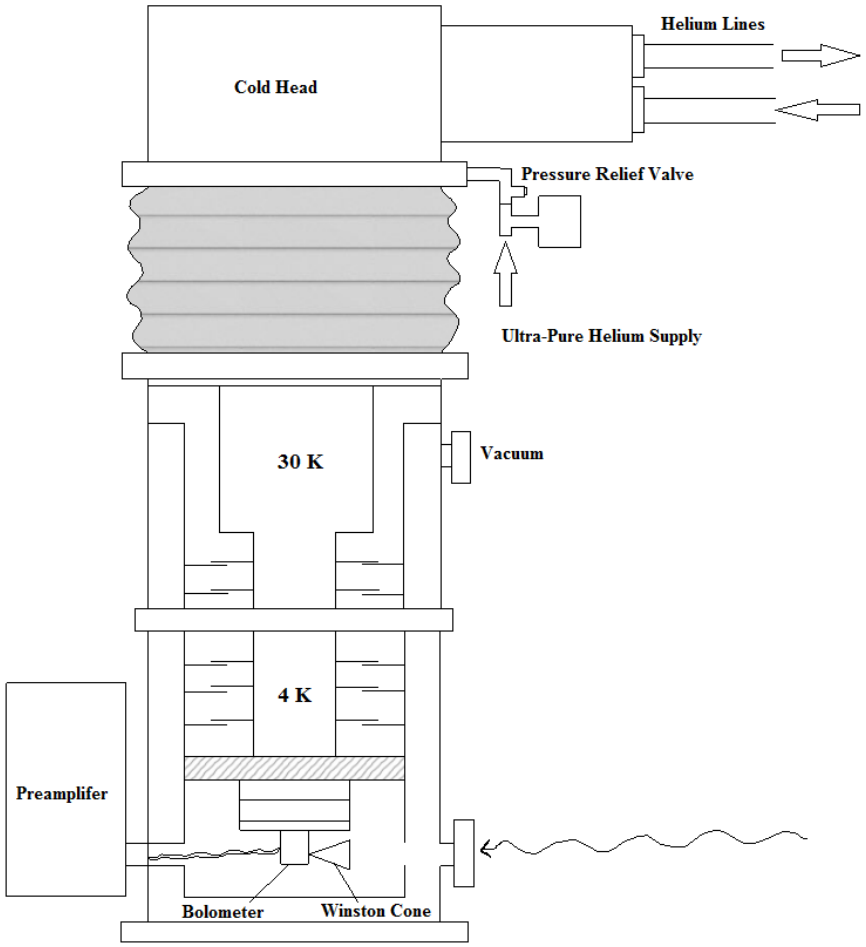

Figure 12. Schematic of the detector. Compressed helium is pumped through the cold head and heat is carried away from the system eventually cooling the system to below 4.2 K.

The cryostat had a 0.75 inch diameter entrance window and there was an internally mounted millimeter-wave feed-horn known as a Winston cone, which directs and concentrates the mm/submm-waves to the detector chip. The InSb detector chip had an active area of 5 x 5 mm^2 in a serpentine layout for increased sensitivity. The InSb chip detects the transient absorption signal for a fixed mm/submm-wavelength. Typical scans were not composed of a single wavelength; instead they consisted of a series of wavelengths over a selected span with the transition being investigated in the center of the span. As the wavelength from the synthesizer was then changed stepwise, the collected spectra are combined to create a Doppler profile based on the time evolving rotational line shapes in frequency domain [30]. An ultra-low-noise preamplifier (QMC Instruments Ltd. Model ULN95) was coupled directly to the cryostat to amplify the transient signals without adding noise.

Output from the preamplifier was then sent via coaxial cable to a second low-noise preamplifier (Stanford Research Systems Model SR560) for a final stage of amplification and frequency filtering, if desired. The conditioned absorption signal was acquired via coaxial cable where the resulting absorption time traces were averaged on a digital oscilloscope (LeCroy Model LC9370), which was then sent to a computer running data acquisition software, LabVIEW®. This program stores relevant experimental parameters, i.e. pressure, reactants, date, time, and is also used to set and step the microwave synthesizer to the appropriate wave probe frequency.

II.C Building of the Apparatus

II.C.1 Previous Setup

The previous molecular beam apparatus of Dr. Duffy's research laboratory was set up for photodissociation experiments, which can be seen in Figure 13 [30]. The photodissociation setup employed a single nozzle that was in a fixed position above the chamber. The nozzle aperture was collinear to the probe millimeter/submillimeter-wave beam and perpendicular to the UV-laser used to dissociate the parent molecules. While this setup was ideal for photodissociation studies, to proceed with the crossed beam reactive scattering studies a new experimental setup was designed and built conjointly with Daniel Mauney, as described herein.

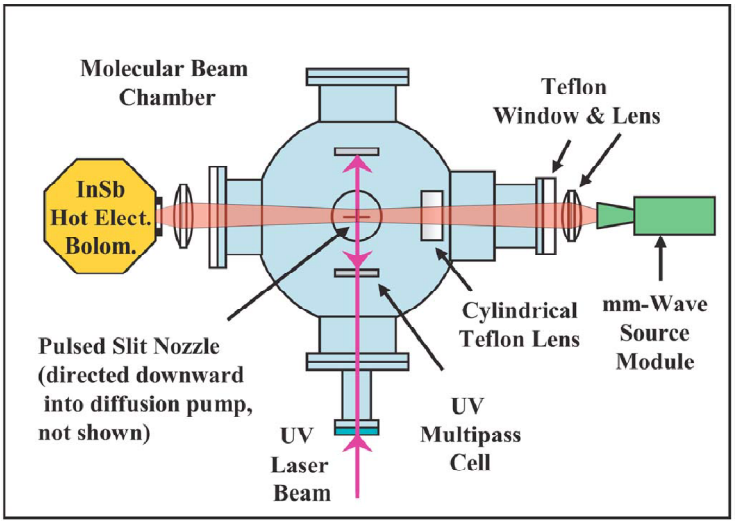

Figure 13. Illustration of the Duffy lab photodissociation setup as viewed from above. The pulsed nozzle is directed down into the vacuum chamber where it is probed via millimeter/submillimeter-waves and detected by the liquid helium cooled hot electron bolometer [30].

II.C.2 Vacuum System

To achieve the high vacuum conditions, 100 mPa to 100 nPa (10^{-4}-10^{-10} Torr), which are necessary to create molecular beams, a multistage vacuum system was employed. The initial step in pumping out the foreline and chamber was done with an Edwards RV12 rotary vane dual stage mechanical pump, which is a positive-displacement pump consisting of vanes mounted to a rotor inside a larger cavity. With a pumping speed of 283 L/min this initial pumping stage can achieve an ultimate pressure of 1.5 x 10^{-3} Torr from atmospheric pressure under ideal conditions. The rotary vane pump was eventually replaced by an Edwards XDS10 dry scroll pump, which consists of two interleaving scrolls, with a pumping speed of 184 L/min. Due to the large volume of the foreline and chamber typically this initial stage was able to achieve a pressure of

~10^{0}-10^{-1} Torr, when this pressure was reached the Edwards EH-250 roots blower, which has a pumping speed of 3992 L/min, was engaged. A roots blower is a positive displacement lobe pump consisting of a pair of meshing lobe rotors that can only pump across a limited pressure differential, which is why the backing pump mechanical pump was necessary. Along with the backing rotary vane or scroll pump the system can achieve an ultimate pressure of 1 x 10^{-3} Torr. Figure 14 shows the scroll pump and roots blower in the labs pump room.

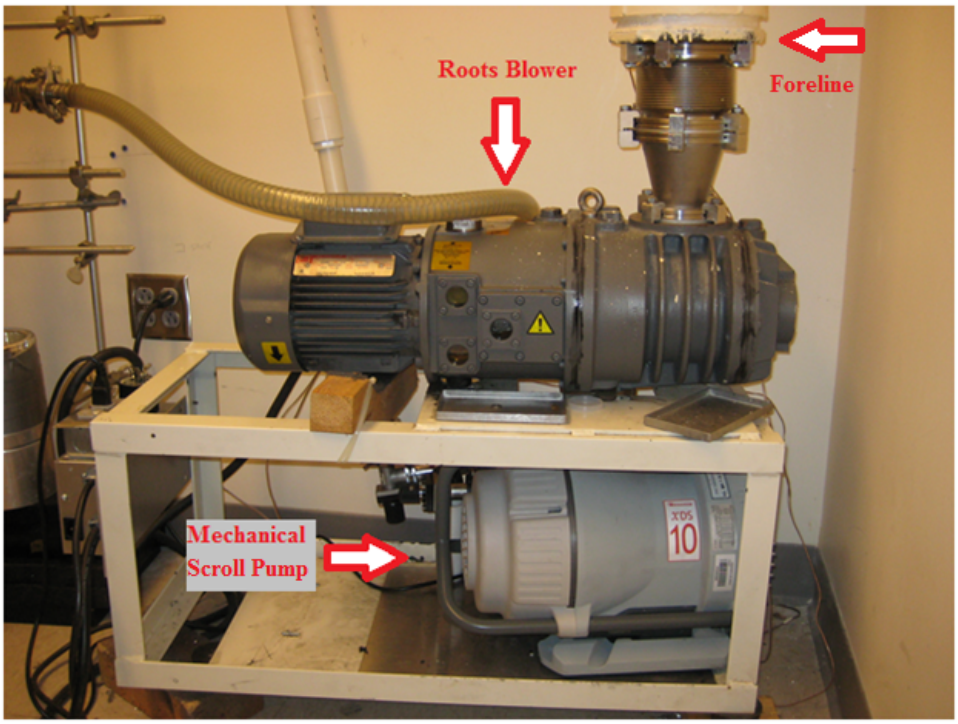

Figure 14. Mechanical pump system. Consisting of roots blower and scroll pump used to achieve typical pressures of 2 x 10^{-2} Torr.

The differentially pumped reaction chamber has a large Varian VHS-6 diffusion pump mounted directly beneath the chamber shown in Figure 15, and a small Leybold-

Heraeus diffusion pump attached to the molecular beam arms above the chamber. Diffusion pumps are a type of molecular pump, with a higher pumping speed than the mechanical pumps described previously, but because of this higher speed they also require a higher vacuum to be established before being used, otherwise the pump will stall/fail. The VHS-6 diffusion pump has a pumping speed of 2,400 L/sec air with an operating range of 1.5×10^{-3} to 5×10^{-9} Torr. The small diffusion pump has a pumping speed of ~75 L/sec air and can achieve an ultimate pressure of 3×10^{-7} Torr under ideal conditions. Once the foreline and chamber are roughed out to a pressure of $\sim 2 \times 10^{-2}$ via the mechanical pumps the chamber can be opened to the diffusion pumps using two gate valves, one on the inlet and one on the exhaust side of the diffusion pump, quickly dropping the reaction chamber pressure to 10^{-6}-10^{-7} Torr.

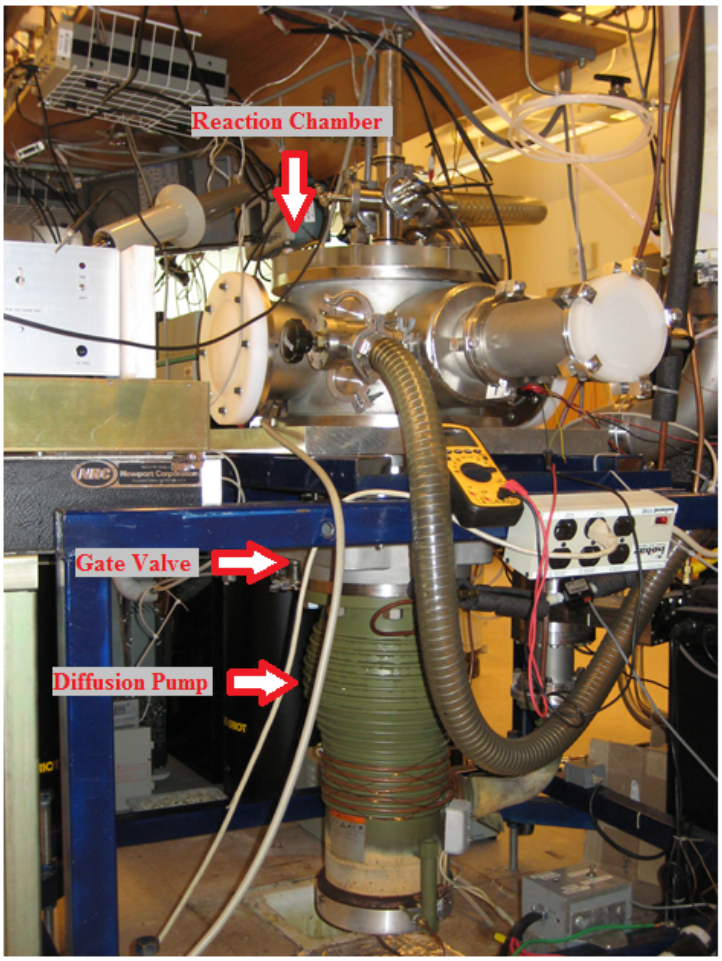

Figure 15. Molecular pump system. Diffusion pump attached directly beneath the reaction chamber and separated with a gate valve to protect the diffusion pump.

The pressure of the vacuum system was monitored using an arrangement of Edwards ATC-E active thermocouple gauges, a Varian (Model 0571-K2471-340) ion gauge and an Edwards active gauge controller, which can be seen in Figure 16.

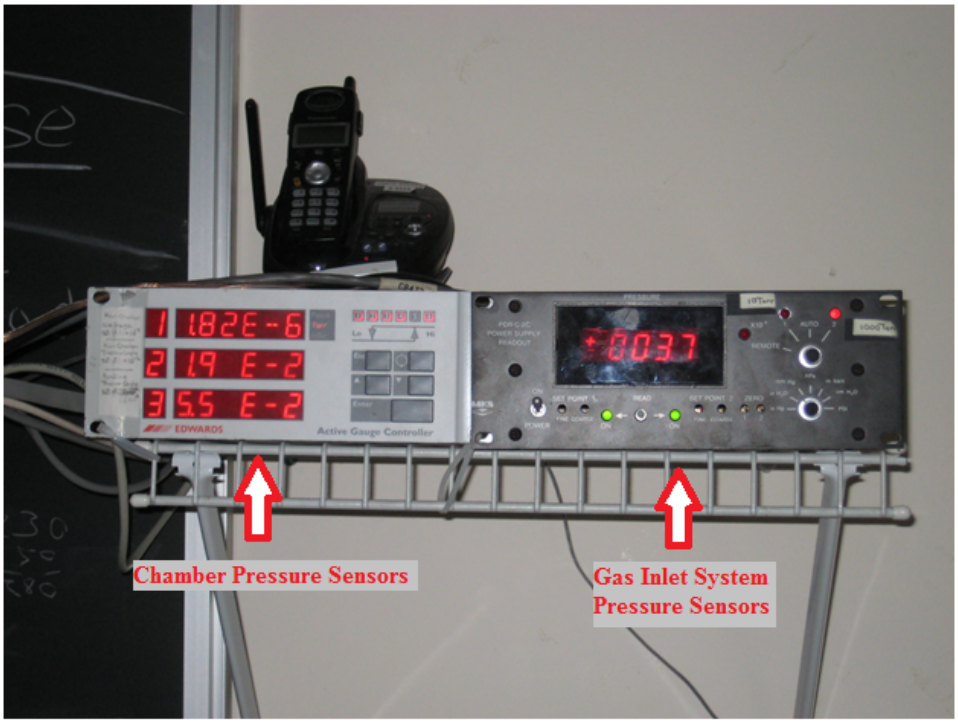

Figure 16. Chamber and gas inlet system pressure sensors. On the left, Edwards active gauge controller monitors three sensors at one time. Channel 1 corresponds to the ion gauge attached directly to the chamber. Channel 2 corresponds to an Edwards active thermocouple attached directly to the chamber. Channel 3 is another active thermocouple attached to the foreline right before the chamber. On the right, MKS Baratron pressure gauge with two channels, this displays the pressure of the gas inlet system.

These gauges are located on various parts of the vacuum system to ensure a proper pump down sequence and that the conditions are ideal for the crossed molecular beam experiments. There are a total of three ATC-E active thermocouple gauges, which are located on the foreline, main chamber and before the mini diffusion pump. Having a thermocouple on the foreline ensured that the mechanical pumps were working properly to create the initial lower vacuum conditions. The thermocouple on the reaction chamber guaranteed that the chamber was properly roughed out before opening the diffusion pump

gate valves, and the thermocouple on the inlet of the mini diffusion pump showed that the molecular beam arms were being pumped on. Because the thermocouple gauges only have a working range down to 10^{-2} Torr, a Varian Bayard-Alpert ion gauge was attached to the chamber to measure the high vacuum conditions in the reaction area.

As a safety measure these pressure sensor signals were tied into an interlock system, which can be seen in Figure 17. On the controller a high and low set point pressure could be programmed for each channel and at these pre-established set points the controller relays a signal to the interlock system.

Figure 17. Interlock system. The five buttons on the left turn on/off the pumps and open/close the gate valves on the chamber. The left four buttons are tied to the pressure and water flow sensors so that if there was a spike in pressure or the water cooling the diffusion pump stopped, which could damage the pumps, the entire system will shut off.

The interlock system allowed for all of the pumps and gates to be turned on/off easily and in a single location. When the appropriate pressure readings were reached for each step of the pump down sequence, the system could be interlocked so if a step was done in the wrong order or conditions that could damage the pumps occurred the system would automatically shut everything off. Having this system in place allowed for the vacuum system to be left on continuously, eliminating the time needed to bring the chamber down to conditions ideal for producing molecular beams and without the possibility of damaging the pumps.

II.C.3 Gas Inlet System

Along with the new chamber design a new gas inlet system was designed to suit the dual nozzle setup needed for crossed molecular beam experiments. Figure 18 displays a schematic of the gas inlet system.

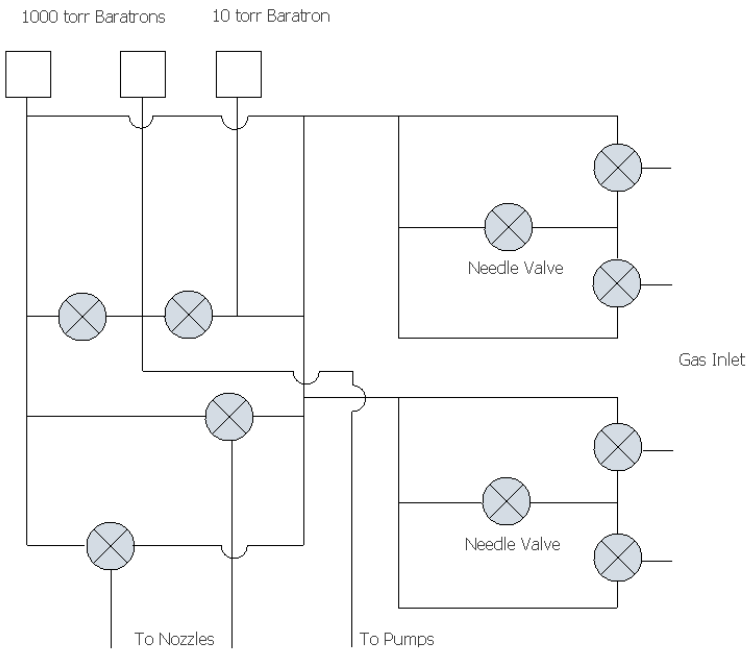

Figure 18. Illustration of the new gas inlet system. There are three baratrons represented by squares, two 1000 torr and one 10 torr, which can be used to measure the pressure in the different sections. A connection to the pump system is made to safely evacuate the system when needed. Four inlet valves will be used to introduce and mix multiple gases for reactions, which can be regulated by the labeled needle valves.

The new inlet system allowed for easy mixing of the parent gases with carrier gases, such as helium, neon or argon. These mixtures could then be stored in tanks for use in subsequent experiments. It also allowed for switching between nozzles readily and

measuring the pressure at each nozzle independently; the completed gas inlet system can be seen in Figure 19.

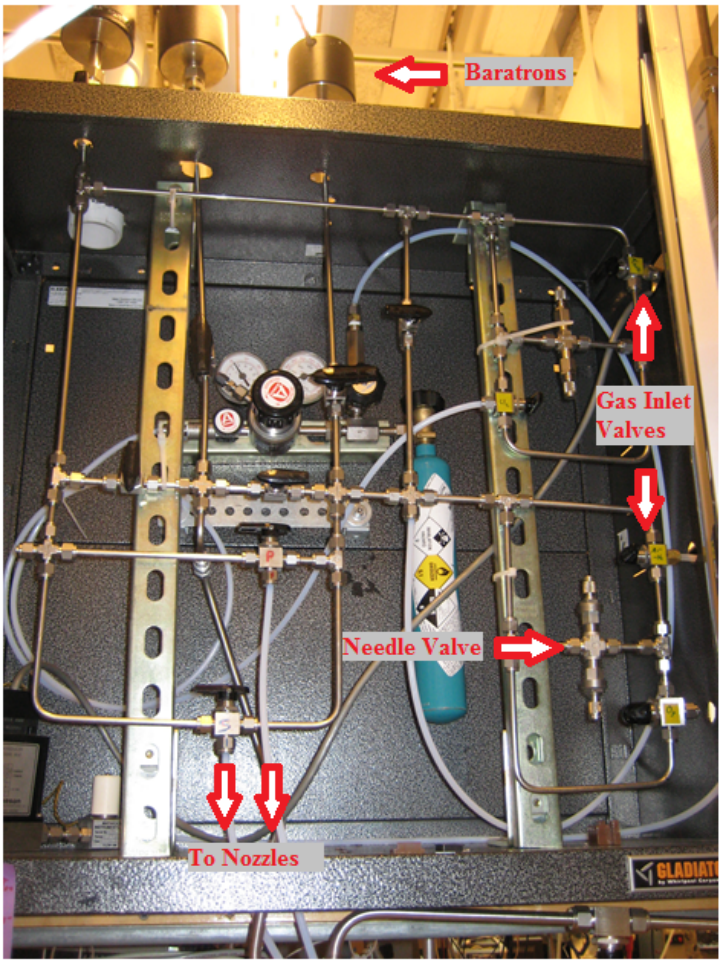

Figure 19. Completed gas inlet system housed in a cabinet.

The gas inlet system was constructed using ¼ inch stainless steel tubing and Swagelok® connections. The entire system can be separated into two distinctive zones, a top and bottom to send gas mixtures to either nozzle without reacting within the tubing. There are four gas inlet valves located on the right-hand portion of the cabinet, which are

connected to other parts of the experimental setup, i.e. ozone, chlorine and carrier gases. These gas inlets can be oriented through needle valves to regulate the stagnation pressure behind the nozzles. Baratrons, located above the cabinet, were used to measure the pressure in the top and bottom zones independently, which are displayed on the MKS (Model PDR-C-2C) pressure gauge shown in Figure 16. The entire system is directly connected to the foreline via 3/8 inch tubing if the system needed to be purged, the larger diameter tubing increases gas flow allowing for a quicker purge. Finally, the entire system has been housed inside a cabinet, which is connected to the buildings exhaust in case of leaks.

II.C.4 Circular System

A later addition to the gas inlet system was the construction of a closed cycle circular system, shown in Figure 20. The development of this system was the reason for the rotary vane pump being switched for the dry scroll pump. Because the scroll pump does not need any oil to run, there is no chance of contamination from oil going into the gas inlet system. When dealing with harsh chemicals such as chlorine, which can react with pump oil and therefore the pump oil would require constant changing, the scroll pump in comparison does not need any special maintenance. Once the high vacuum conditions had been established, the exhaust of the pump system could be switched from a connection to the building exhaust to instead feed back into the gas inlet system. The reason for constructing the circular system was for use in non-reactive scattering experiments where the reactant molecules and carrier gas could be recycled to cut down

on the need to purchase these items regularly. However, using the circular system for the O_3 + Cl experiment would be futile because the highly reactive species involved would be destroyed before ever reaching the circular system.

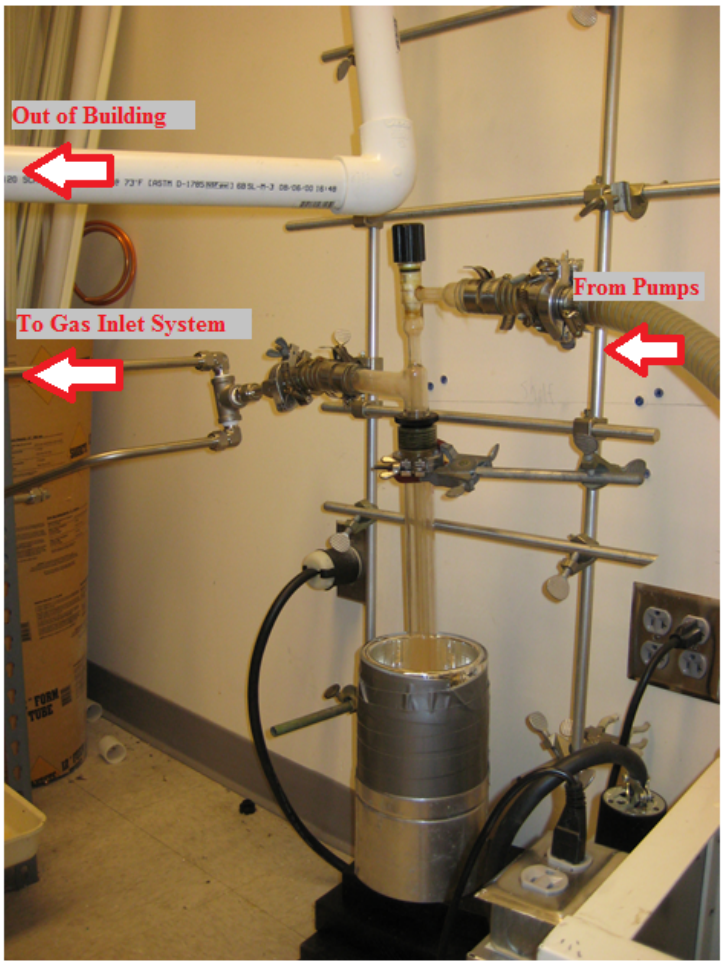

Figure 20. Closed cycle circular system. Exhaust from the pumps can be switched to the closed cycle system to recycle reactant molecules in non-reactive experiments. Typically there is a reservoir tank, not shown, attached to the system to reduce the fluctuation in the stagnation pressure at the nozzles. A glass trap is also included in the system if a reactant molecule needed to be separated and collected from the carrier gas.

II.C.5 Ozone Generation System

It was necessary to prepare and trap the ozone immediately prior to running any reactions due to its being an unstable species that will degrade readily into O_2. Ozone can be generated by various different methods including corona discharge, ultraviolet light, cold plasma or electrolytic methods. For this experiment, it was produced via corona discharge from an ozone generator pictured in Figure 21.

Figure 21. Ozone Generator. Molecular oxygen, set to the appropriate flow and back pressure, is passed through the corona discharge instrument creating ozone. The percentage of ozone output can be controlled from 0 to 100%.

The ozone output from the generator was then passed through a pre-cooling stage, which consisted of coiled tubing placed in an ice water bath, and then it was passed through the glass trap system shown in Figure 22. This trap system consisted of a long glass gas manifold with three gas inlets, one for the ozone output from the generator, one for a carrier gas and one was unused; all gas inlets could be opened and closed with Teflon

stopcocks. This inlet glass tube was connected to a glass trap filled with silica gel, which was cooled to approximately -78˚C using a dry ice/acetone bath [9,32-34] (not shown).

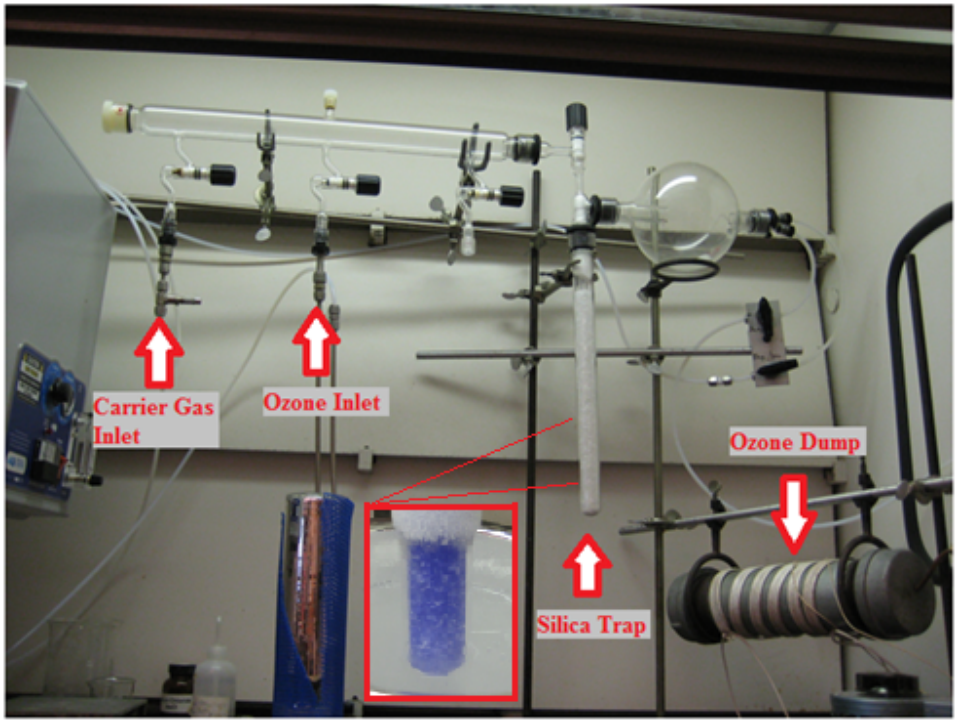

Figure 22. Glass trap system for the collection of ozone. Ozone is produced and then subsequently trapped on silica gel (shown in the insert), which can then be sent either to the gas inlet system or the ozone dump.

The gas trap system was connected to the gas inlet system using ¼ inch Teflon tubing. It was important to use Teflon tubing when dealing with ozone because other materials such as stainless steel will react with the ozone and destroy it before it reaches the reaction chamber. The silica trap was also connected to an ozone dump. To increase the destruction of ozone being sent to the dump, it was heated using heating tape

connected to a variable transformer, which allowed the temperature to be regulated based on the current being sent to the heating tape.

II.C.6 Chamber Arm Construction

The first step of the new setup was to design and build the freely rotating arms, which hang from the top of the reaction chamber, shown in Figure 23.

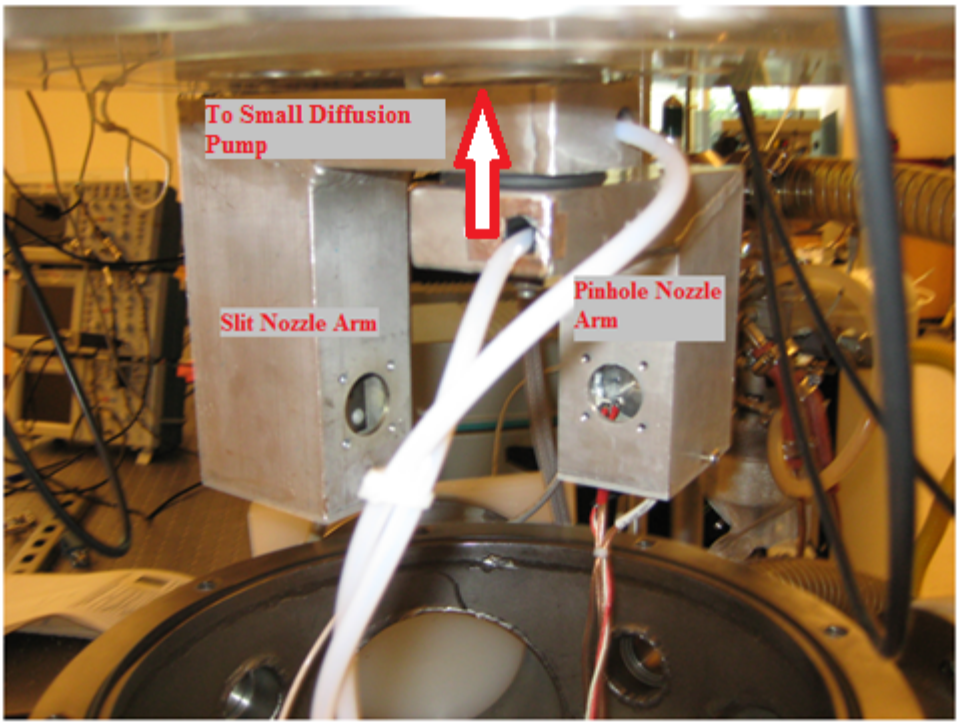

Figure 23. Rotatable nozzle arms, which are suspended from the chamber lid.

It was important that the arms were precisely designed so that the molecular beams crossed directly in the middle of the chamber. Because the design called for the arms to be able to rotate independently of one another, one arm was designed to be longer than the other, while still accounting for a spacer and O-ring between the two. The arms were

constructed from two pieces of square aluminum tubing with the dimensions shown in Figure 24 and 25.

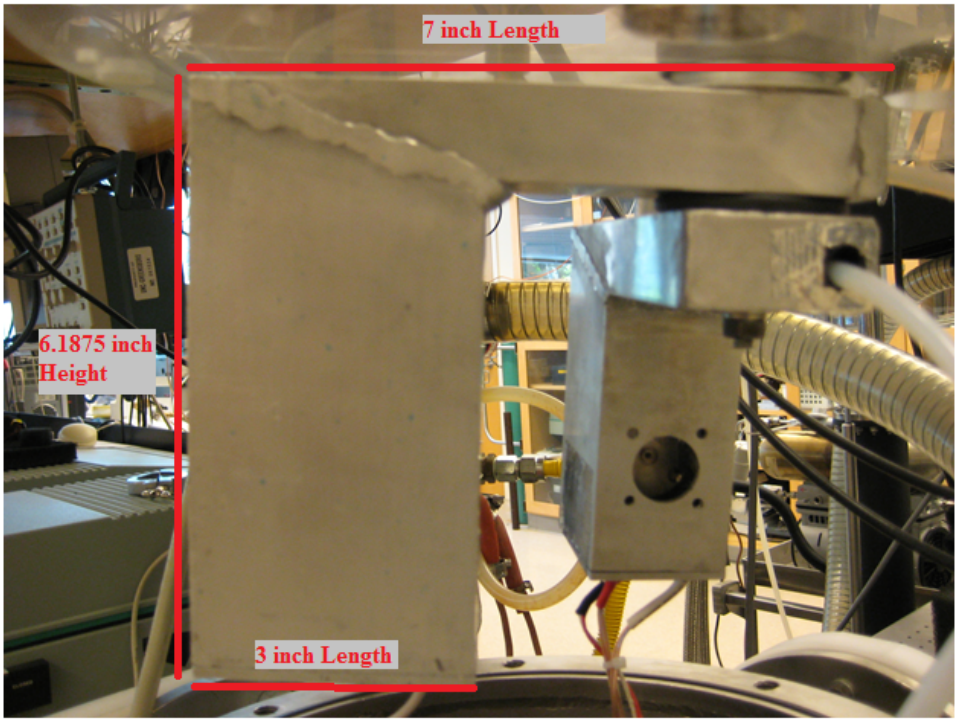

Figure 24. Large rotating arm dimensions. Not shown is the 2 inch width of the arm. The increased height of this arm accounts for the 2/16 inch spacer and O-ring between the two arms.

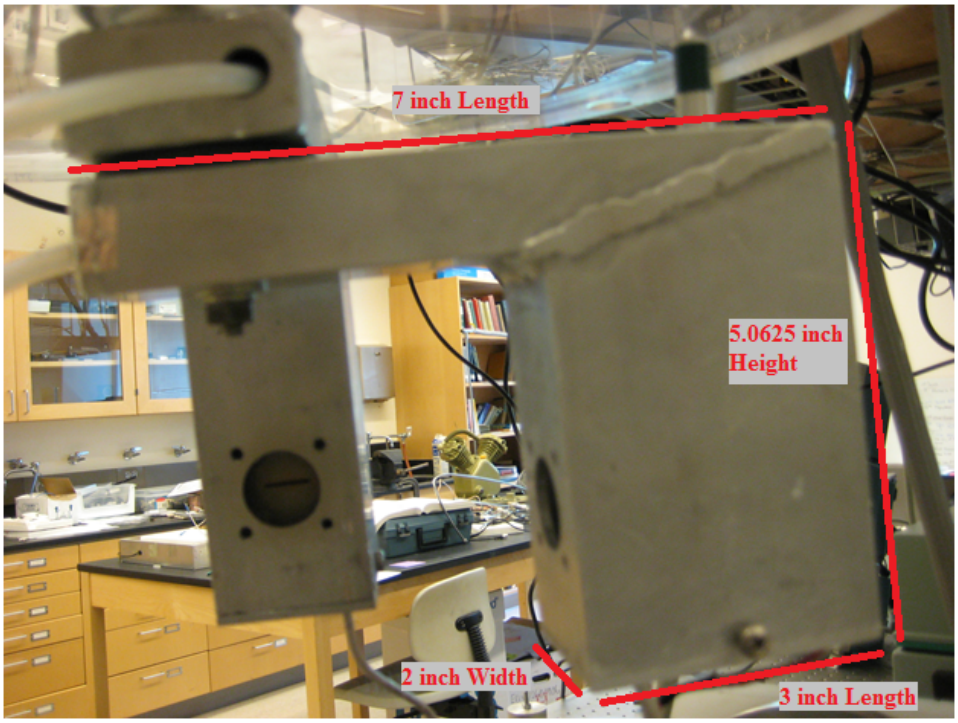

Figure 25. Small rotating arm dimensions. Note that the dimensions are identical to the larger arm except for the height.

The arms were connected to the exterior chamber via a threaded tube protruding from the middle of the chamber lid. Initially this was connected to a polyvinyl chloride (PVC) spacer piece; however it was realized that this piece had a tendency to leak, which raised the ultimate pressure the vacuum system could establish. Therefore, a new piece was milled and threaded from a solid aluminum rod resulting in a more robust and secure connection. This spacer piece was directly connected to the larger arm and could be used to rotate it without needing to open up the chamber. From this spacer piece, a six-way cross is affixed as shown in Figure 26. From the top of the six-way cross, a metal rod was placed down the center of the entire arm system and was directly connected to the smaller arm. This rod not only secured the entire design but also allowed for the smaller

arm to be rotated without needing to open up the chamber. The mini diffusion pump was also connected to the six-way cross to create the differentially pumped conditions inside the arms. Eventually the conductance of the arms was determined to be not large enough, so holes were drilled into the bottom of the arms to further facilitate the removal of background gas molecules in the arms. One of the other connections of the six-way cross is used for vacuum electrical feed-through connectors between the nozzles and the pulse driver, and another connects to the high voltage discharge system. Initially the gas inlet system lines were fed through this cross but eventually the gas feed tubing to the nozzles was switched to outside the arm system to increase the throughput area to the mini diffusion.

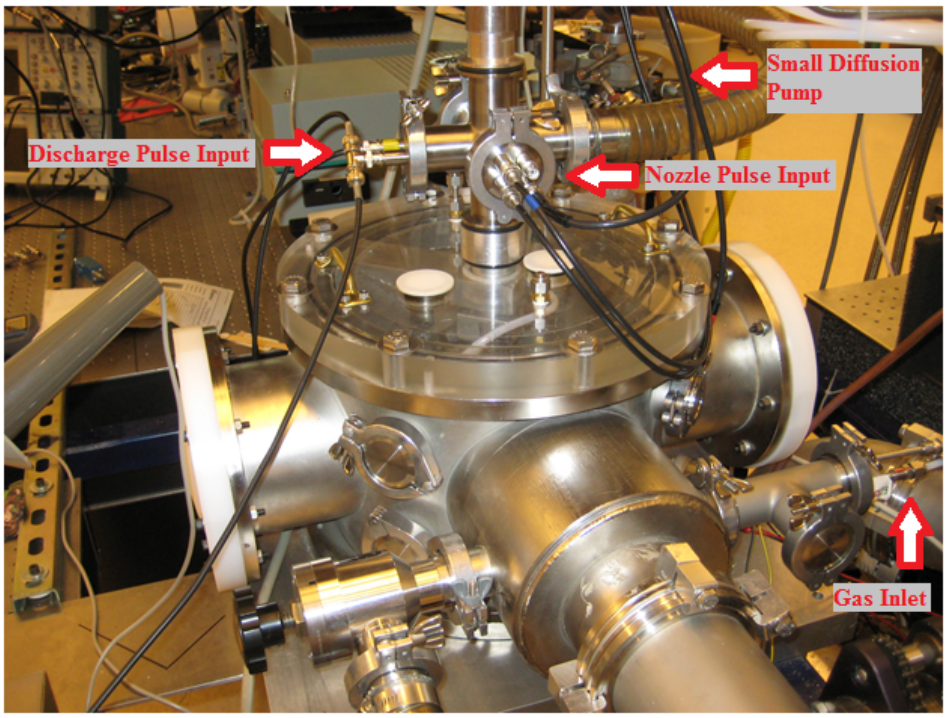

Figure 26. Reaction chamber. Connections to the nozzles and discharge plates were made using coaxial cables.

This setup allowed for independent rotation of the arms around the chamber facilitating reacting parent molecules at a wide range of angles, which allowed the relative kinetic energy of the reactants to be adjusted easily. In a fixed arm apparatus, the relative kinetic energy of the reactants can only be adjusted by changing the expansion conditions of the molecular beams. This has the undesired effect of changing the initial reactant internal state distributions, and hence complicates the analysis of the resulting data. To know what angle the arms were at the chamber lid was etched, this can be seen in Figure 27.

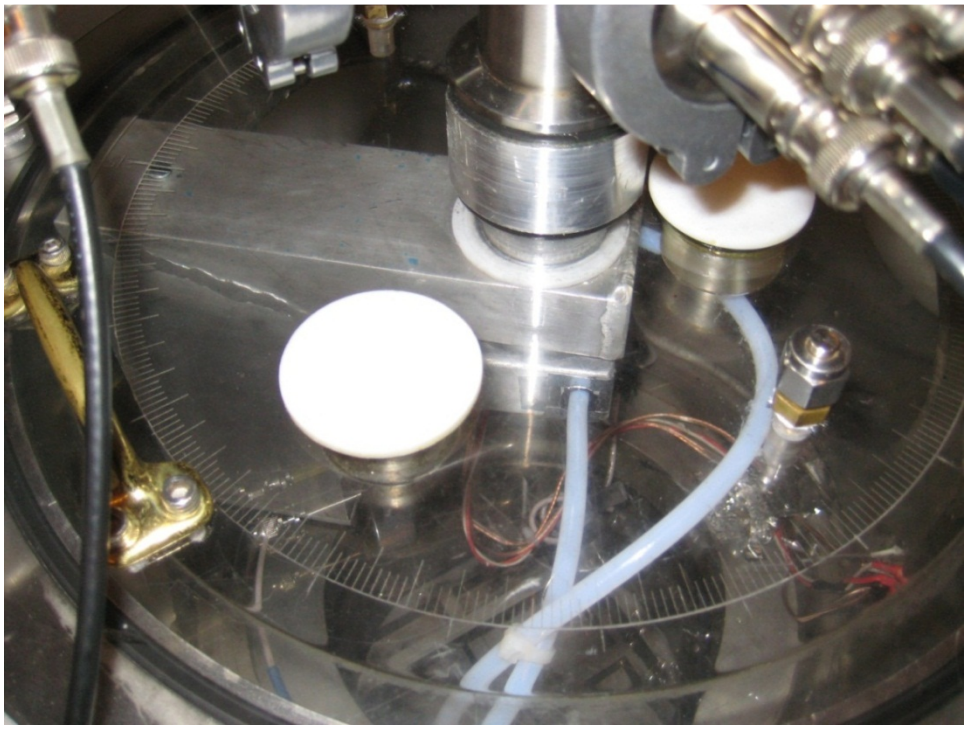

Figure 27. Etched chamber lid. The chamber lid has been etched so that the angle of the arms with respect to the experimental setup could be measured. Each mark is a degree, with the full 360° technically available although certain angles would block the mm-waves, with every five degrees marked using a medium sized line and every fifteen degrees represented by the longest mark.

II.C.7 Nozzle Construction

Each of the two arms contained one of the available nozzles that were used to pulse the gas, either neat or a mixture, into the chamber. One of these nozzles has a pinhole opening while the other has a slit opening. When using neat gas the intermolecular forces can cause clustering, which can result in the formation of droplets but this can be remedied using a carrier gas. The pinhole nozzle and skimmer pulses the gas in a three-dimensional cone shape, which is displayed in Figure 28.

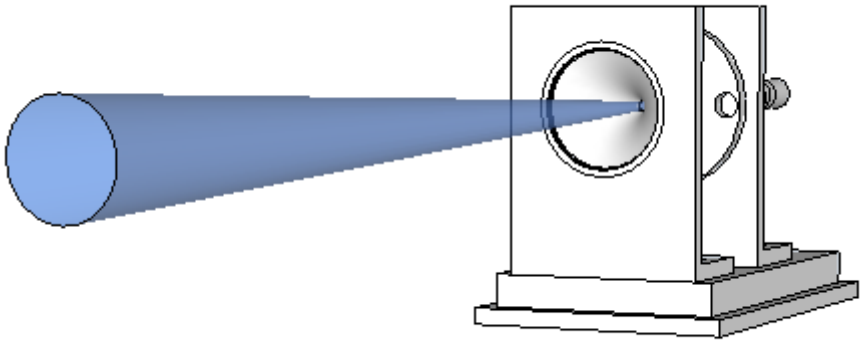

Figure 28. Pinhole expansion. Profile is symmetrically cone shaped about the flow axis, shown through a skimmer.

Compared to the slit nozzle the pinhole puts out a lower density of gas with a larger angular spread. Because of this there tends to be less cooling and clustering of the gas from the pinhole nozzle, and hence a larger percentage of the parent molecule relative to the carrier gas can be used. The slit opening pulses the gas in a two-dimensional sheet with a much higher density of gas but a smaller spread, as seen in Figure 29.

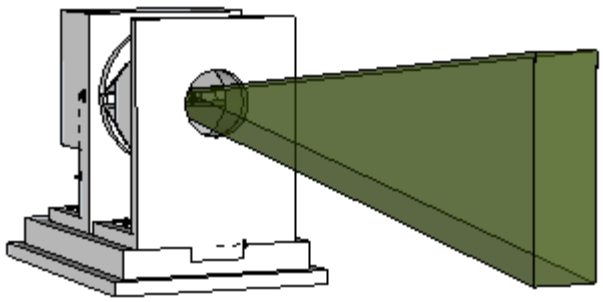

Figure 29. Slit expansion. Profile is rectangular in cross-section. Although not shown, the slit is oriented horizontally. The expansion profile for the slit nozzle is not symmetrical with the spread perpendicular to the nozzle being larger than the spread parallel to the nozzle's slit axis.

These conditions lead to more clustering of the gas beam, which can be remedied by careful choice of a carrier gas and stagnation pressure. Along with the temperature and pressure of the source gas, the carrier gas will also dictate the terminal velocity of the beam as shown in Figure 30 [4,31].

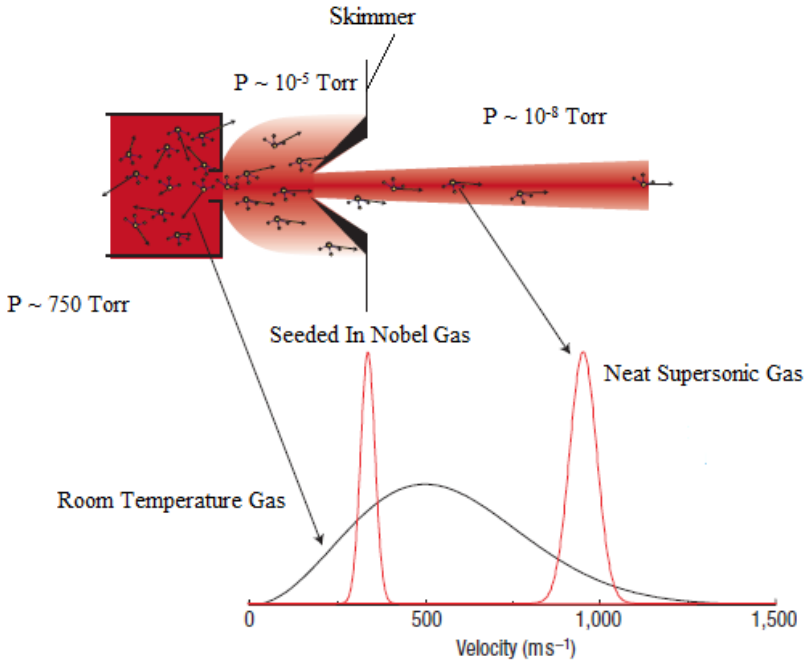

Figure 30. Effect of supersonic expansion and use of a carrier on the velocity distribution of a gas. Top: Illustration of supersonic expansion. High pressure gas is expanded into a differentially pumped vacuum system through a small orifice and then through a skimmer. Bottom: Velocity distributions are shown for the neat supersonic beam and room-temperature. Using a noble gas as a carrier will narrow the velocity distribution compared to the pure gas however the velocity will be dictated by the carrier gas [adapted and reprinted with permission from Nature Publishing Group].

Due to the small space available in the rotating arms, to fit the nozzles some alterations were made. The original nozzles from Parker can be connected to a gas system via a compression fitting on the back. To fit the nozzle into the arm, this compression fitting was removed and the resulting hole was sealed. A new inlet hole was drilled perpendicular to the original opening and this hole was threaded. A connector piece was milled from stainless steel rod to connect the new nozzle opening to the gas inlet system.

II.C.8 Pinhole Nozzle - Ozone

Ozone is an ideal reactant because it is a polar molecule it can be detected using the direct absorption of mm/submm-waves. The pinhole nozzle was used to create the ozone molecular beam. With the smaller volume of gas and larger spread, it was believed that this would be ideal in decreasing the formation of ozone dimers and clusters. However, when first tested minimal to no signal from the ozone was detected. Based off a previous study [9], the nozzle needed to be heated to ~80°C to reduce the formation of dimers.

The initial attempt to heat up the nozzle was done using a resistance wire, which was coiled round the body of the nozzle. The resistance wire proved unable to heat up the nozzle to the required temperature. The next attempt to heat up the nozzle was done using a pair of ceramic resistors, 15 Ω and 39 Ω. Both of the resistors were rated to 5 watts and using the equation $P = \frac{V^2}{R}$ the maximum power that could be put across them was 5 W. Typical power needed to heat the nozzle up to ~80°C was 3.3 W while in the vacuum chamber, and voltage across the resistors was controlled with a Mastech DC Power Supply (Model HY3005F-3). The temperature of the nozzle was monitored using a thermocouple wire, Type J (iron and copper-nickel), attached to a multimeter. Using this heated nozzle setup, ozone was detected, however the peak was broadened due to the heating of the molecules.

II.C.9 Slit Nozzle - Chlorine

Atomic molecular beams from molecular precursors can be produced using various methods, including laser photolysis, rf or microwave discharge, or pyrolysis by heating of the nozzle [9,35-37]. For this experiment, a double stage pulsed discharge technique was attempted to create the atomic Cl similar to that used by Ren [38]. The chlorine (Cl_2) gas mixture was to be passed between a series of alternating metallic and Teflon plates as seen in Figure 31. As the gas was pulsed through the plates it was to be subjected to two pulsed discharge regions, a lower current preionization region and a high current main discharge region. Having an initial preionization stage was supposed to be advantageous in creating a partially ionized seed species to stabilize and increase the efficiency of the subsequent main discharge downstream. The two stage discharge was later abandoned for a simpler method, which will be described in the next section.

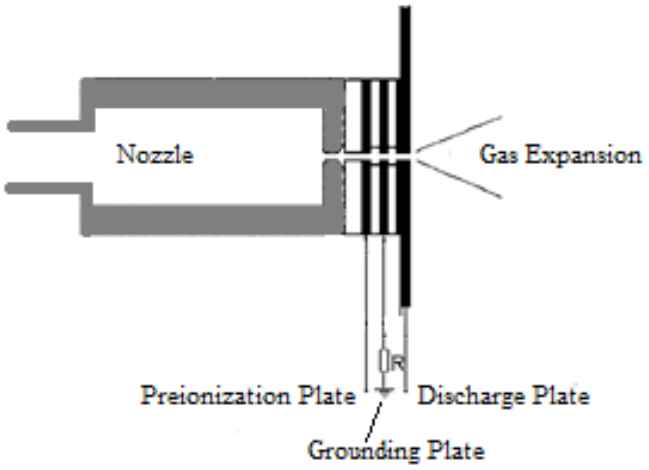

Figure 31. Schematic of the discharge nozzle. A series of alternating Teflon (white) and metal (black) plates are connected directly to the nozzle. The preionization and discharge plates are labeled with a grounding plate between

The alternating plates were attached to the front of the nozzle with nylon screws to isolate the high voltage from to the grounded nozzle. It was important to align the opening of each plate with one another to ensure the path for the gas was unhindered. The discharge and grounding plates each had extending tabs where the high voltage or grounding wires were attached, and they were oriented in the best way as to reduce the possibility of arching from plate to plate. The grounding wire was run down and out from the bottom of the rotating arm and affixed to the chamber. As mentioned earlier, the two high voltage wires were run up through the six-way cross so that they could be connected via coaxial cables to the discharge circuit box. The assembled discharge plate setup can be seen in Figures 32 and 33.

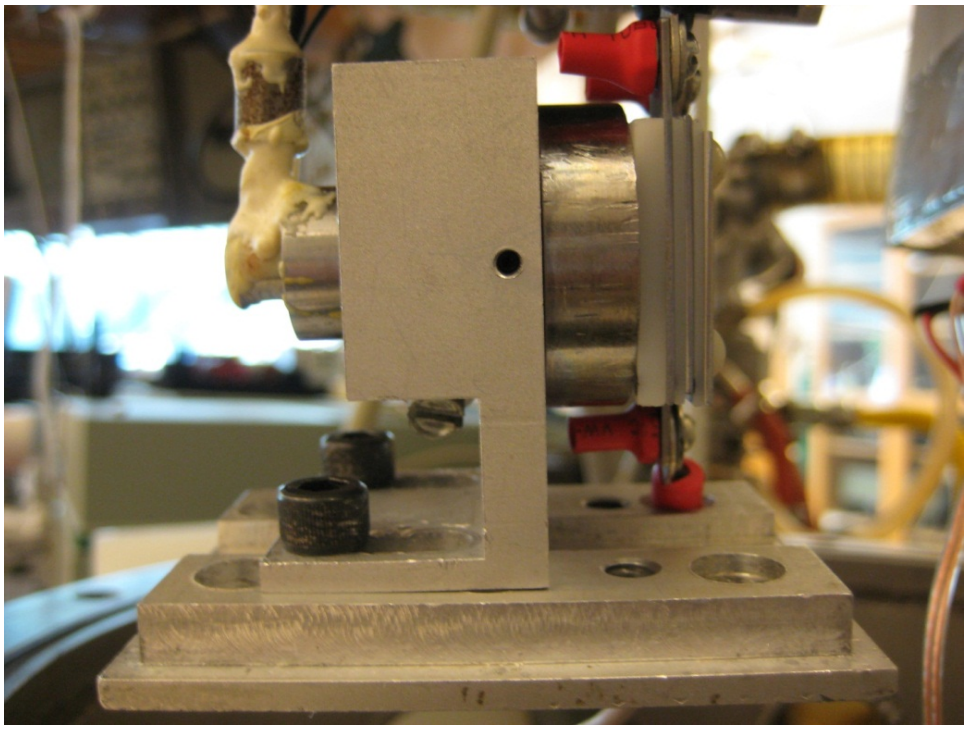

Figure 32. Side view of the slit nozzle with discharge plates attached. The final assembled nozzle is very similar to the schematic shown above with alternating Teflon and stainless steel plates. The thickest of the Teflon plates is located right against the nozzle face to provide a large buffer region so that the discharge current does not go back to the nozzle.

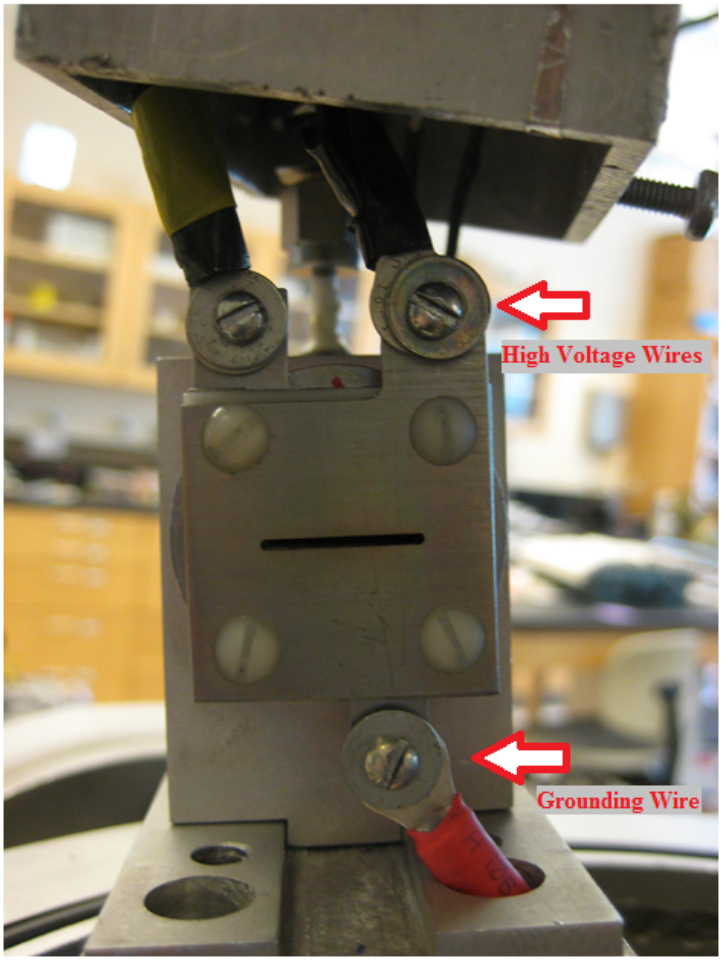

Figure 33. Front view of the slit nozzle with discharge plates. The plates are aligned to provide a free path for the molecular beam. The grounding wire is run down through one of the holes in the bottom of the arm and is attached to the chamber. The high voltage wires are run up through the rest of the arm system.

II.C.10 Discharge Circuit

The circuit attempted for the two stage discharge sequence was similar to that used by Ren [38]. High voltage input was produced by a Glassman High Voltage Inc. MR Series power supply, which had been modified to produce positive voltage and had a

maximum output of 1500 V. This high voltage was sent into a circuit box constructed in-house, Figure 34, and through a 47 Ω power resistor.

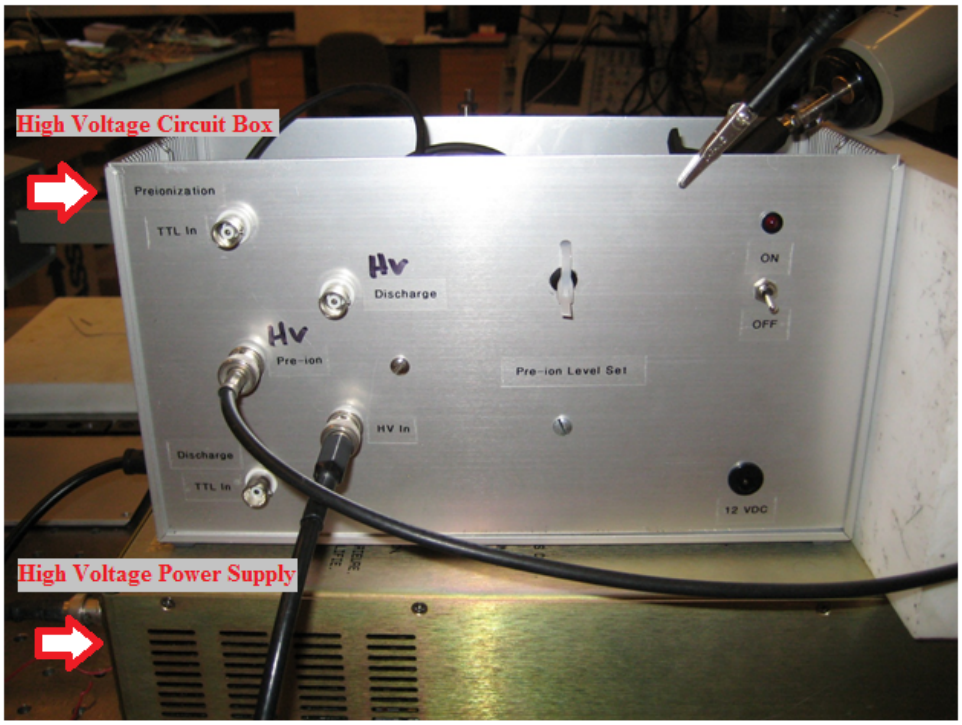

Figure 34. High voltage circuit box and high voltage power supply. The power supply produces the high voltage, which is attached to the circuit box where it is split into a pre-ionization and main discharge [51].

After the resistor there was two fast high voltage transistor switches, one was purchased commercially, Alphalas HVS Series, and the other was constructed in-house [51]. These switches were controlled using a TTL pulse from the Berkley Nucleonics Corp. (BNC) Model 555 Pulse Generator. The pre-ionization pulse lasted for 10 μsec, and it was then sent through a 25k Ω variable resistor, allowing the pre-ionization stage to be adjusted to create the best conditions for discharge. For the main discharge pulse, there was a 10

μsec delay after the pre-ionization stage and then it was pulsed for 1 μsec without a resistor after the switch.

While running the initial trials of the discharge system the high voltage was monitored using a Tektronix P6015A 1000:1 voltage probe. It was noticed that the Alphalas high voltage switch was not working properly and was always allowing high voltage to pass through instead of the 1 μsec discharge period. Because of this, the Alphalas was replaced by another switch made in-house. After the replacement of the switch, a new problem occurred with the nozzle not firing properly at the high voltage conditions. It was thought that the high voltage was arcing through the gas back to the nozzle face to ground. In an attempt to fix this an additional thick Teflon plate was added between the original discharge plate sequence to increase the distance between the nozzle and high voltage plates, and a Teflon disk, in which a slit was cut to match the slit of the nozzle, was attached to the nozzle face plate, however the firing problem remained. Misfiring of the nozzle was later determined to be due to the rf interference created by the discharge. This rf was causing the BNC 555 pulse generator to not work properly, which in turn caused the nozzles to fire improperly. Because of this, the firing of the nozzles was switched to the Parker IOTA One Valve Driver. The pulse sequence was eventually abandoned because the high voltage switches failed, and a design in which there was constant high voltage on the discharge plates was adopted.

In this setup, which can be seen in Figure 35, the two high voltage transistor switches were bypassed and the high voltage was attached through a 47 Ω resistor to limit the current draw from the Glassman high voltage supply and then to a 25k Ω variable

resistor directly to the discharge plates. Eventually the variable resistor was replaced by a 1k Ω power resistor after the variable resistor failed. With this new circuit the expected current across the discharge plates was 500-700 mA. This constant voltage system was then tested and gave a more uniform discharge across the entire slit opening, however when the voltage was probed it was noticed that for every gas pulse the voltage in the circuit dropped substantially, ~150-250V, so there was some time needed to recover to the set voltage due to the Glassman power supply having a 200 mA max current. To solve this problem a series of capacitors, 1350 V and 40 μF, was added after the 47 Ω resistor to store charge and it prevented the large drop in voltage seen previously. Figure 36 shows the internal parts of the discharge circuit box.

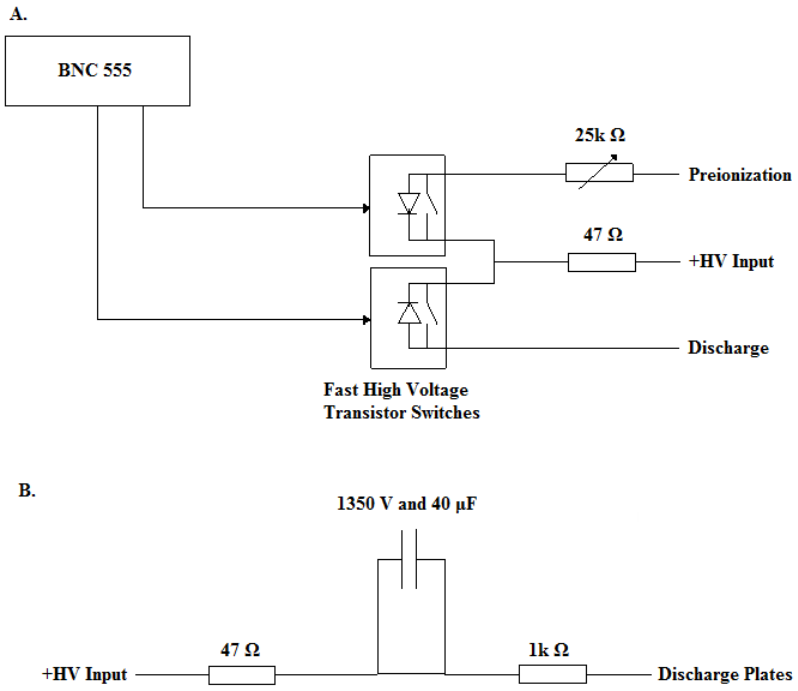

Figure 35. Schematic of the discharge circuit. A. Original circuit with fast high voltage transistor switches controlled by the BNC 555 pulse generator. B. Circuit with transistor switches bypassed and inclusion of capacitors.

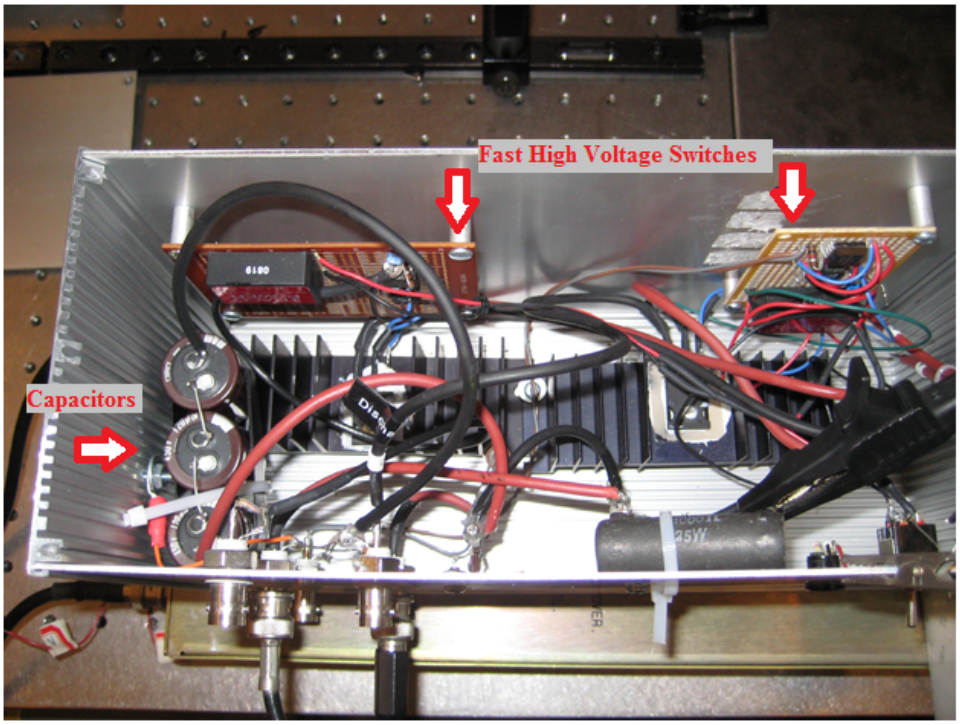

Figure 36. Internal view of the discharge circuit box after the switches were bypassed and variable resistor removed. The two in-house fast high voltage transistor switches are attached to the wall of the box and large black heat sinks can be seen on the bottom. The capacitors, three 450 V, 120 μF, are wired in series on the left.

II.C.11 Lenses

When dealing with the mm/submm-wave system it was important to take into account the beam optics and geometry of the setup. The location of lenses, with varying focal lengths, and the source can be used to alter where the beam waist is located to create the most ideal conditions [39]. Using two lenses the mm/submm-waves were focused with a Gaussian beam telescope geometry so that the beam waist was at the middle of the chamber, increasing the intensity right at the reaction center, while ensuring that the beam waist is independent of wavelength. This was done by placing the lenses

so that the focal lengths of one lens and the next meet at the same point. The first lens located after the mm/submm-wave source was made of polymethylpentane (TPX), which is a transparent polymer, and has a focal length of 6 inches. The other two lenses are spherical lenses and were turned on a lathe from high-density polyethylene (HDPE). They were mounted directly to the ends of the chamber, and the one on the source side has a focal length of 10.5 inches, while the lens on the detector side has a focal length of 21 inches. The setup from the source through the first lens and into the chamber can be seen in Figure 37. After the second lens attached to the chamber, the mm/submm-waves were directed towards the detector window.

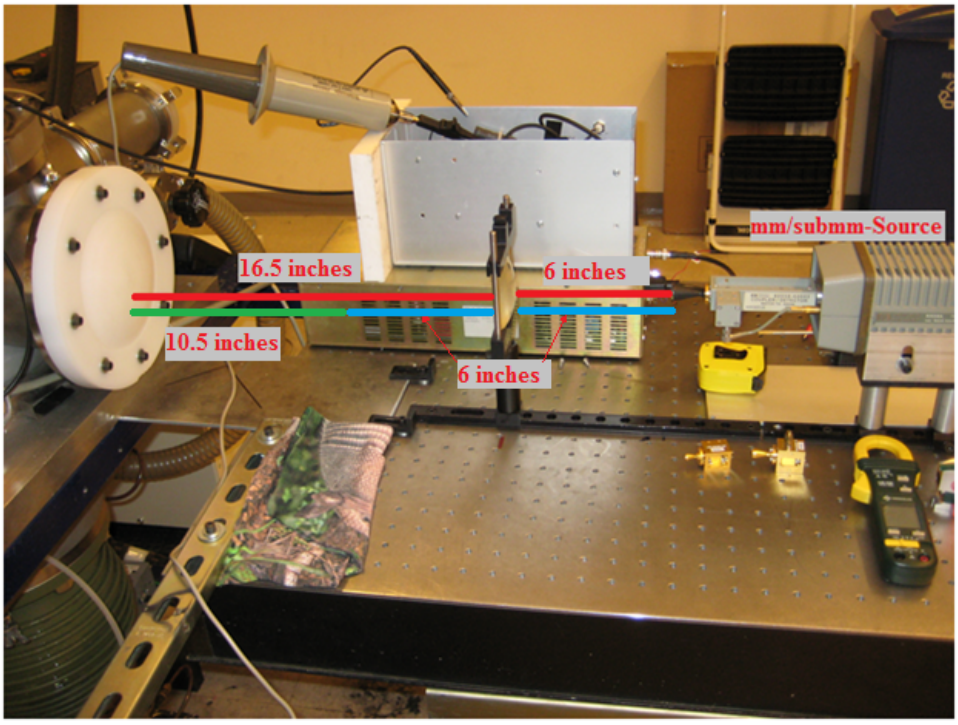

Figure 37. Lens setup from the source to the chamber. The mm/submm-waves are focused through the first lens, which has a focal length of 6 inches (blue lines), and then to the lens attached to the chamber, which has a focal length of 10.5 inches (green line). The total distance from lens to lens is the sum of the focal lengths of the individual lenses.

II.C.12 Detector

Initially the InSb detector chip used in the Dr. Duffy's lab was housed in a liquid-nitrogen/helium Dewar made by Infrared Laboratories Inc. (Model HDL-5). When experiments were run this Dewar needed to be filled with liquid nitrogen and liquid helium every time because eventually it would boil off. With the rising cost of helium a new closed cycle system, consisting of a cold head, compressor, gas lines and low vibrational interface designed by ColdEdge Technologies, was implemented. Figure 38 shows the detector as it is set up in the laboratory.

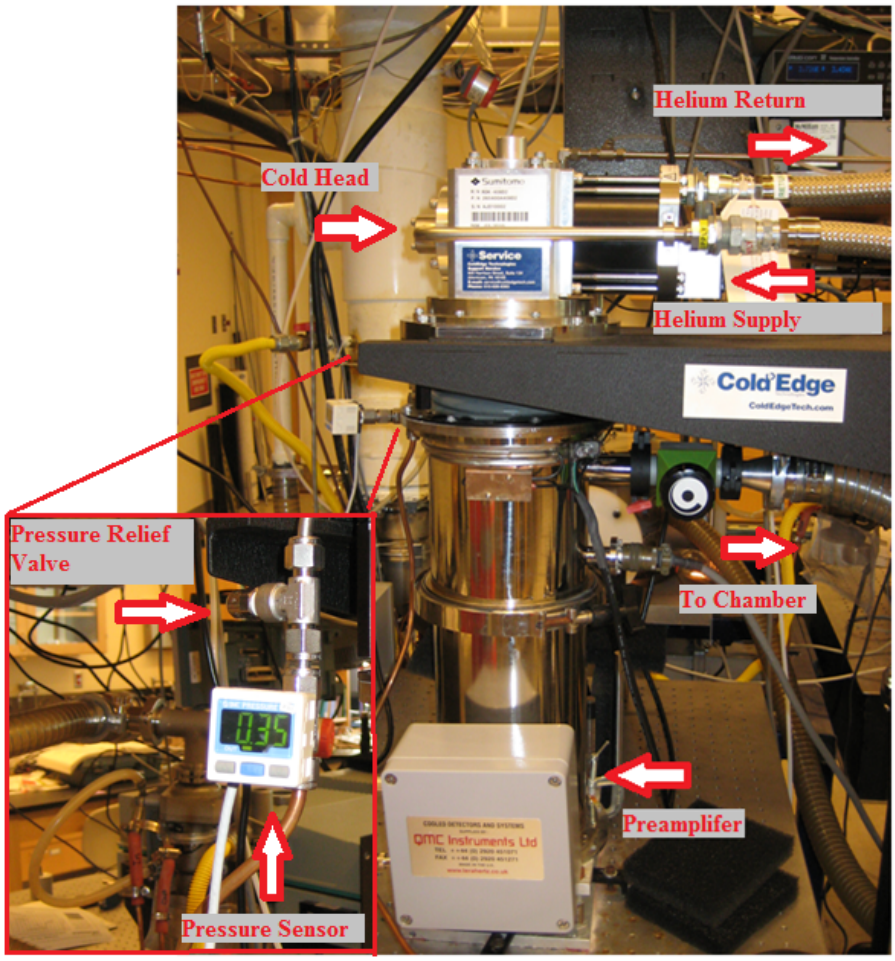

Figure 38. Detector setup. Cold head located at the top is connected with helium lines to the compressor. Pressure sensor measures the helium flow into the detector.

In the closed cycle system, high-pressure helium gas from the compressor is transferred via the gas lines to the cold head. In the cold head, the incoming gas is cooled by regenerators as it passes through. The gas exits the regenerator assembly and then passes through the motor housing and finally exits the cold head to return to the compressor. Expansion of the helium gas in the displacer-regenerator provides the cooling for the two-stages, 30 K and 4 K, of the cryostat. A sampler holder, where the

InSb chip is located, is mounted to the low vibration interface, which is connected to the cryostat. Two temperature sensors are strategically placed near the detector chip to accurately measure the temperature and they can be monitored using the Cryo-con Model 32 temperature controller made by Cryogenic Control Systems Inc., shown in Figure 39.

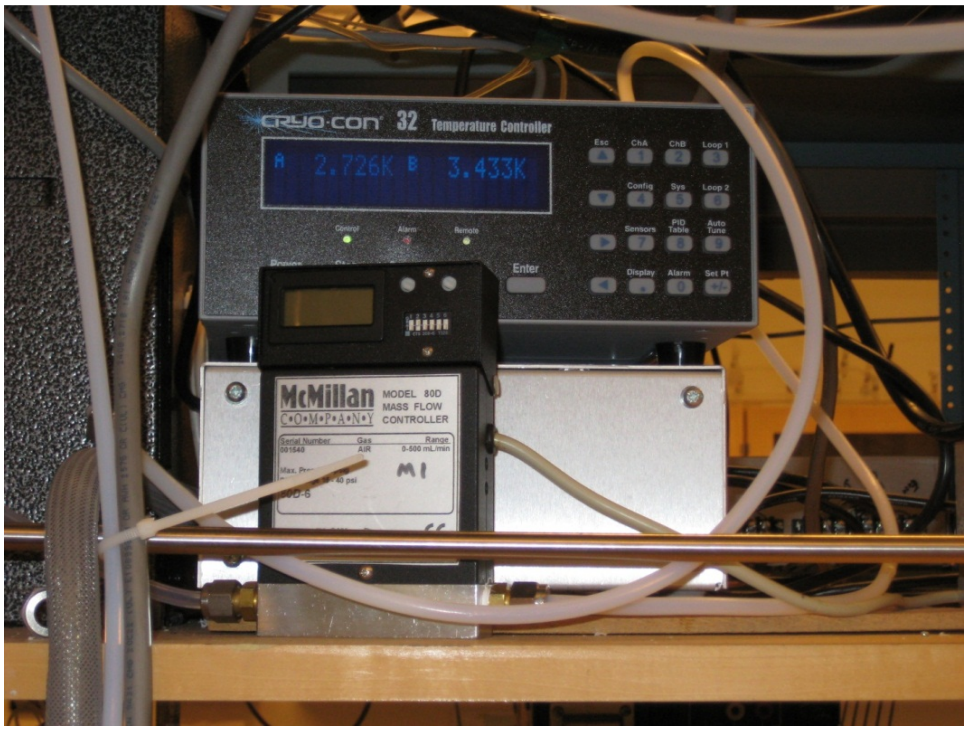

Figure 39. Temperature controller used to show the temperature at the InSb chip in the detector. The temperatures shown on the controller are typical for the completely cooled down system where the experiments can be conducted.

The displacer assembly, sample holder and low vibration interface are all placed in a vacuum shroud, which acts as an insulator between the sample area and ambient conditions. Having these in the shroud also ensures that there will be no ice buildup inside the detector.

II.C.13 Cool-Down Sequence for the Detector

The cool down of the detector from room temperature typically required two to three hours to reach temperatures below 4.2 K. The first step was to evacuate vacuum shroud. This was done by opening a valve on the detector, which was connected directly to the main reaction chamber. A vacuum of 10^{-3} Torr was needed before the system was turned on; if this pressure is not reached there could be a buildup of ice inside the shroud. Once the temperature of the detector dropped below 150 K, the detector could be sealed off from the pump system. At this temperature, the cold head creates its own vacuum via cryo-pumping.

Once the vacuum shroud had been evacuated the low vibration interface needs to be purged of any air that may be trapped inside, this was done using ultra-pure, 99.999%, helium. A ½ psi flow of the ultrapure helium into the detector was also needed during the cool down. The reason for the addition of helium is that the heat exchangers on the cold head and heat exchangers on the low vibration interface mate without physically touching. The helium fills the space between these exchangers and as the cryostat is cooled down it cools down the helium gas, which cools down the detector chip.

As a convenience and protective measure an interlock system was designed where the pressure of the helium going to the detector was regulated to ½ psi using a 524C 2-stage LP regulator, shown in Figure 38, and a SMC pressure switch (Model ISE30A) was mounted to the helium inlet line on the detector, which can be seen in Figure 35. This pressure switch was used to monitor the pressure of the helium entering the detector. If abnormal conditions occurred, such as a drop in pressure, the pressure switch would shut

off the compressor and cold head. Had the compressor and cold head been allowed to continue to run, the bellows on the detector would be sucked in which could damage the detector. There is also a pressure relief valve located after the pressure switch. The purpose of the relief valve is so that if a high pressure of helium builds up in the detector it will be released. High pressure can cause the bellows to explode, tear or blow out from underneath their flanges, which again would damage the detector. Typically once the detector has been cooled down all the way it can be left running as long as there is proper water flow to cool the compressor and a proper flow of helium to the detector.

II.C.14 Warm-Up Sequence for the Detector

Should the detector need to be shut off it was ideal to collect the ultra-pure helium to use in the subsequent cool down. A simple system was designed, displayed in Figure 40, to pump the helium from the detector into two large reservoir tanks. The warm up process usually required two to three hours to complete and the system had to be monitored continuously to ensure the pump did not cause the bellows to suck in.

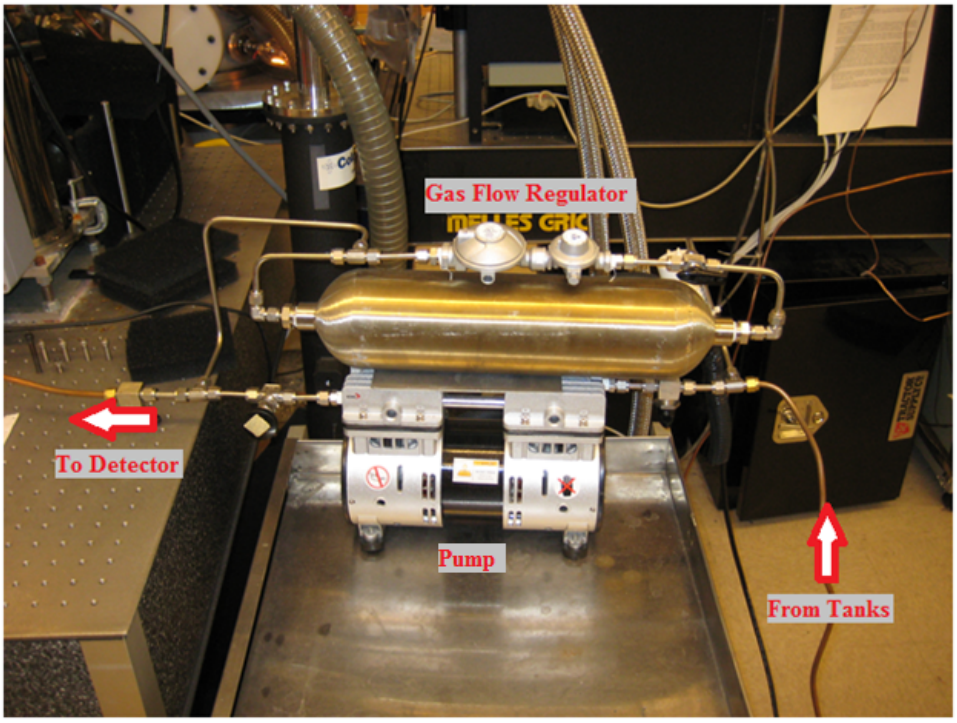

Figure 40. Helium inlet system going to the detector. The helium flows from tanks through a gas flow regulator, which has an output of ½ psi. The regulator can be bypassed through a ballast tank if a higher flow of helium is needed. A pump located underneath the ballast tank can be used to collect the helium during a warm up procedure.

II.D Experimental Difficulties

It is worth mentioning that when designing and building a new instrument, many unforeseen problems can arise. During the course of the construction of the new apparatus, there were numerous complications that occurred that delayed the system from being completed. One of the largest complications occurred in the modification and upgrade of the detector to a closed cycle system. The detector was supposed to be gone for only twelve weeks during the construction and testing of the system. However, there were numerous delays and it ended up taking twelve months to be returned and when it

finally arrived the entrance window was not lined up with detector chip. A copper spacer needed to be milled to lower the InSb chip to the level of the entrance window. Although copper is normally a great thermal conductor, the detector chip was not able to reach a temperature of 4.2 K. To solve this indium foil was sandwiched between the surfaces of the copper spacer, which finally resulted in the detector reaching its minimum temperature of 3.4 K.

Our original detector chip was damaged by QMC during the design process and as a result a new one was provided. When the detector was then tested to get initial measurements about the sensitivity and responsivity, the new detector chip sent was bad and only worked intermittently. Therefore, it was sent back to the manufacturer, which further delayed testing a little over a month.

Further complications with the detector system involved fuses in the ultra-low noise preamplifier going bad and needing to be replaced, as well as one of the helium lines in the closed cycle system leaking. When this occurred, most of the helium in the lines and compressor leaked out and the entire system needed to be recharged using ultra-pure helium and the line was replaced.

To run the compressor for the closed cycle detector system, chilled water was used to keep the compressor from overheating. However, the chilled water lines proved to be not operational during the cold months of the year and the detector needed to be turned on and off in the same day. The combination of these typically took 5-6 hours, leaving minimal time to run experiments.

The power amplifier for the mm/submm-wave source, which allows the use of the doubler and tripler, was damaged and sent to be repaired. During this time, only the fundamental range of frequencies for the source was available to be used. Finally, the 220 V plug that powers the large diffusion pump was singed due to the material not being able to handle the large current and was replaced with a plug that could handle the specifications.

CHAPTER III

RESULTS AND DISCUSSION

III.A Experimental Data

III.A.1 Modeling of Molecular Beams

Three-dimensional models of the molecular beams described herein were constructed with equations taken from Demtröder [40]:

$$n(v_z) = C_1 e^{\left(\frac{-m(v_z-u)^2}{2kT_{\parallel}}\right)} \tag{3.1}$$

Equation 3.1 is the Gaussian velocity distribution along the flow axis (moving away from the nozzle) of the gas pulse, which is dependent upon the molecular mass, *m*, and translational temperature parallel to the flow velocity, $T_{/\!/}$, which describes the width of the distribution. Similarly, equation 3.2 is the velocity distribution perpendicular to the flow axis is described with respect to the molecular mass and the translational temperature, $T_{\perp}$.

$$n(v_x) = C_2 e^{\left(\frac{-mv_x{}^2}{2kT_{\perp}}\right)} = C_2 e^{\left(\frac{-mv^2 sin^2\epsilon}{2kT_{\perp}}\right)} \tag{3.2}$$

The velocity of the flow along the z-axis, v_z, is parallel to the mean beam velocity along the z-axis, u, while v_x is the flow perpendicular to the flow velocity. In both of these equations, k is the Boltzmann constant. When the gas pulse is being skimmed, a collimation ratio can be characterized by using equation 3.3.

$$\frac{v_x}{v_z} = \tan\epsilon = \frac{b}{2d} \tag{3.3}$$

The collimation ratio is the ratio between the skimmer diameter, b, and the distance from the nozzle to the skimmer, d.

Due to the pinhole and slit nozzle having different expansion profiles, as shown in Figures 28 and 29, the velocity distribution equations were altered accordingly. The pinhole nozzle has a symmetrical cone expansion about the flow axis, this results in an equal expansion along the x- and y- axes. In this case, equation 3.2 can be used for velocities along the y-axis without any alterations to get a full three-dimensional distribution. However, the slit nozzle with a box shaped expansion will not have equal x- and y- components. Therefore, the y- component in equation 3.2 was modified to account for the rectangular cross-section of the expansion. Three-dimensional models for the slit and pinhole nozzle can be seen in Figure 41.

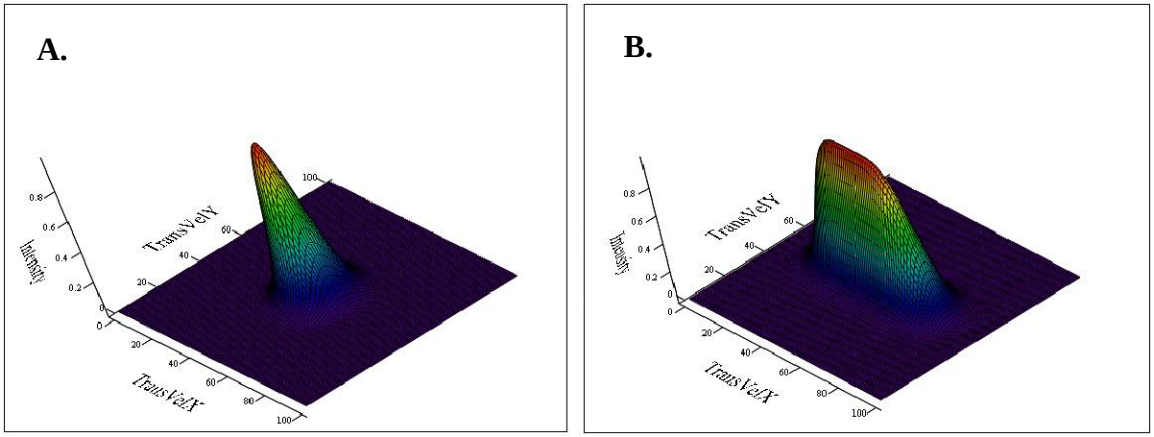

Figure 41. 3D model of velocity distributions for pinhole (A.) and slit (B.) nozzles perpendicular to the flow axis.

III.A.2 Slit Nozzle Studies

Since the slit nozzle has a different expansion profile depending on its orientation, vertical or horizontal, a study was conducted to determine which orientation would be better for further crossed beam experiments. To eliminate Doppler broadening due to the molecular beam angle, the slit nozzle was oriented perpendicular to the mm/submm-wave source. Scans were done on the J=6←5 N_2O, the theoretical transition frequencies used are from NASA's Jet Propulsion Laboratory Spectroscopy Database [41]. Transitions between the rotational energy levels for a diatomic (rigid rotor) molecule, such as N_2O, follow the specific selection rule, $\Delta J = \pm 1$.

From these scans, Figure 42, Doppler broadening based on the expansion can clearly be seen. When the slit nozzle is oriented horizontal, A and B in Figure 42, the signal is centered on the transition with a small amount of broadening in the frequency domain. However, when the slit is oriented vertically, C and D, the signal peak is much

wider in the frequency, over 0.4 MHz. Because it is ideal to have the reactants with a narrow distribution, in frequency and time, the horizontal orientation was used for further experiments.

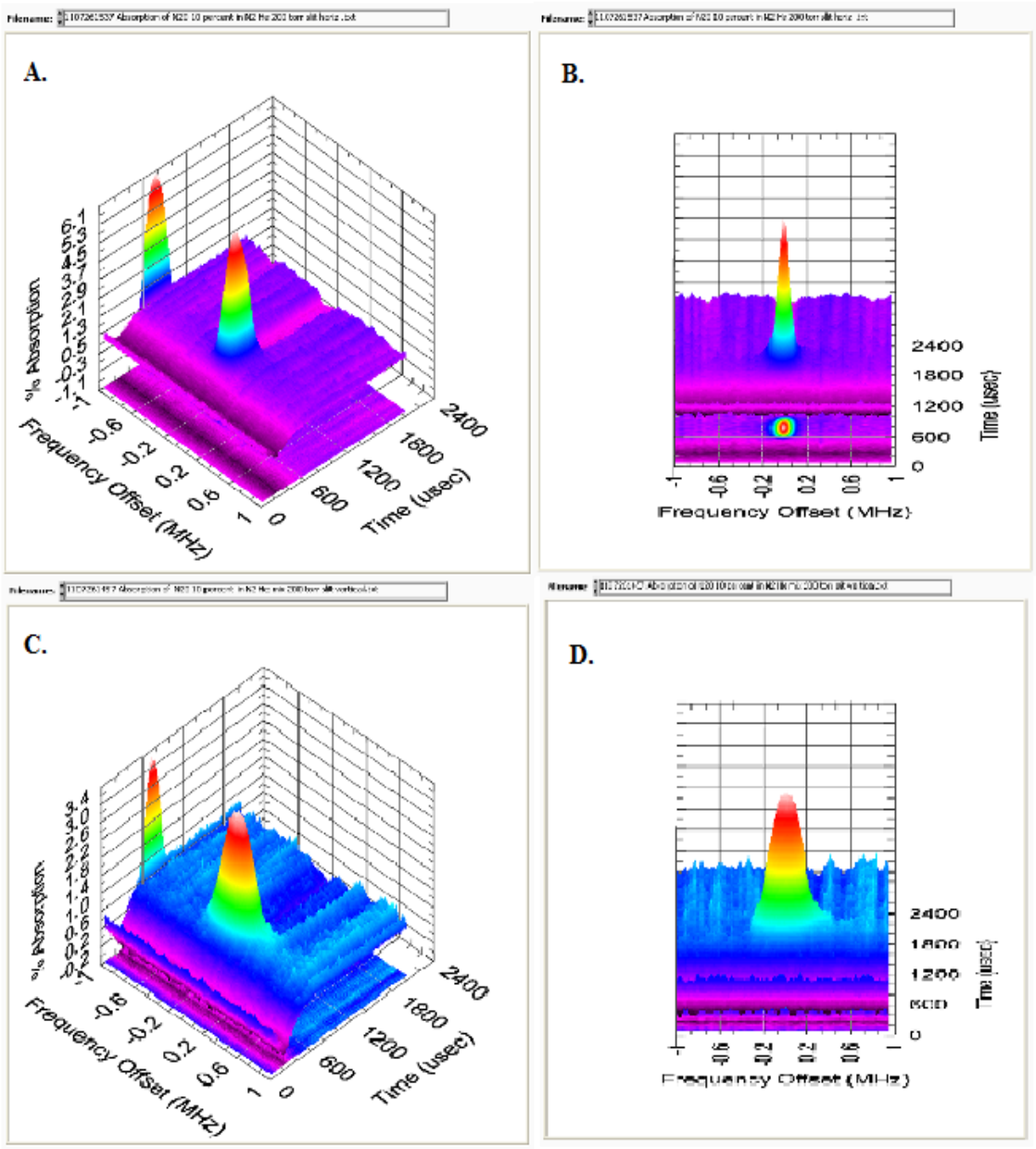

Figure 42. Slit orientation scans of the J=6←5 transition of N_2O. Center frequency is 150135.0460 A. Horizontal slit. B. Frequency offset of horizontal slit. C. Vertical slit. D. Frequency offset of vertical slit.

III.A.3 Ozone Studies

Testing the nozzle expansion profiles was done with ozone. As previously mentioned, there was no signal originally seen from the pinhole nozzle probably due to clustering and it was later heated to solve this issue. Scans of the pinhole nozzle, set perpendicular to the mm/submm-wave source, expansion can be seen in Figure 43. For these scans, a background was first taken. During the background scan the nozzle was fired normally, without gas, so any systematic artifact that resulted from the firing of the nozzle or other noise could be subtracted out subsequently. In these scans there is a larger narrow, in frequency and time, peak of ozone seen at the earliest point of time. This peak corresponds to fastest portion of the molecules with a translational temperature of ~77 K, but the peak is only ~100 μsec in length, which is far too short for the 550-600 μsec pulse length. However, the scans also show a portion of molecules with a weaker signal probed later in time, which has a longer length in time of ~550-600 μsec. This portion has a transitional temperature of ~122 K; this difference is likely a result of the heating of the nozzle. We speculate that early in time the heating of the nozzle appears to be successful in reducing clustering resulting in the sharp peak. As time goes on, the expansion becomes steady state and the cooling from expansion is more efficient. Therefore, clustering likely increases in the middle of the beam and monomer signal is depleted, so possibly only ozone on the fringes of the molecular beam is being measured.

Ozone used in these scans was between 20-30% with an initial pressure of ~150-200 torr before being seeded in argon to a final pressure of ~650 torr. Scans of varying pulse lengths (550 and 650 μsec) were done to see if there was a dramatic increase in the

reactant signal, which could improve the probability of a reactive collision. The increase in pulse length correlated to an increase in ozone detected in the slower portion of the signal, however there was little difference in the fastest portion.

Identical experimental conditions were also done using the slit nozzle, Figure 44. In the slit scans there is only a single broader, in frequency and time, peak compared to the pinhole scans. The broader peak is a result of the larger volume of gas, which is pulsed from the slit nozzle. As the pulse length (550, 600 and 650 μsec) was increased, the width of the peak also showed an increase. Also, when the pulse length was increased from 550 to 600 μsec there was a large increase in the size of the ozone signal, but when the pulse length was again increased to 650 μsec the size remained fairly consistent. This consistency is likely due to the nozzle firing dynamics. The nozzle resonates differently when different opening times are applied, so the nozzle does not respond in a linear correlation in time to the programmed pulse length.

Because ozone is a triatomic molecule, it has a more complex rotational motion than the simple diatomic rigid rotor. Ozone is an asymmetric-top molecule, which is a rotor where no two principal moments of inertia are equal [42]. The behavior of an asymmetric molecule leads to complex energy levels, which can be examined most simply using oblate and prolate systems. The notation for describing an asymmetric-top molecule must be designated using the total angular momentum of the molecule, J, and the angular momentum of an axis, K. Since there are two different axes, the value of K is further separated into K_{-1} for the prolate and K_1 for the oblate [42]. Thus, notation for a single energy level for ozone will be represented as J_{K-1K1}.

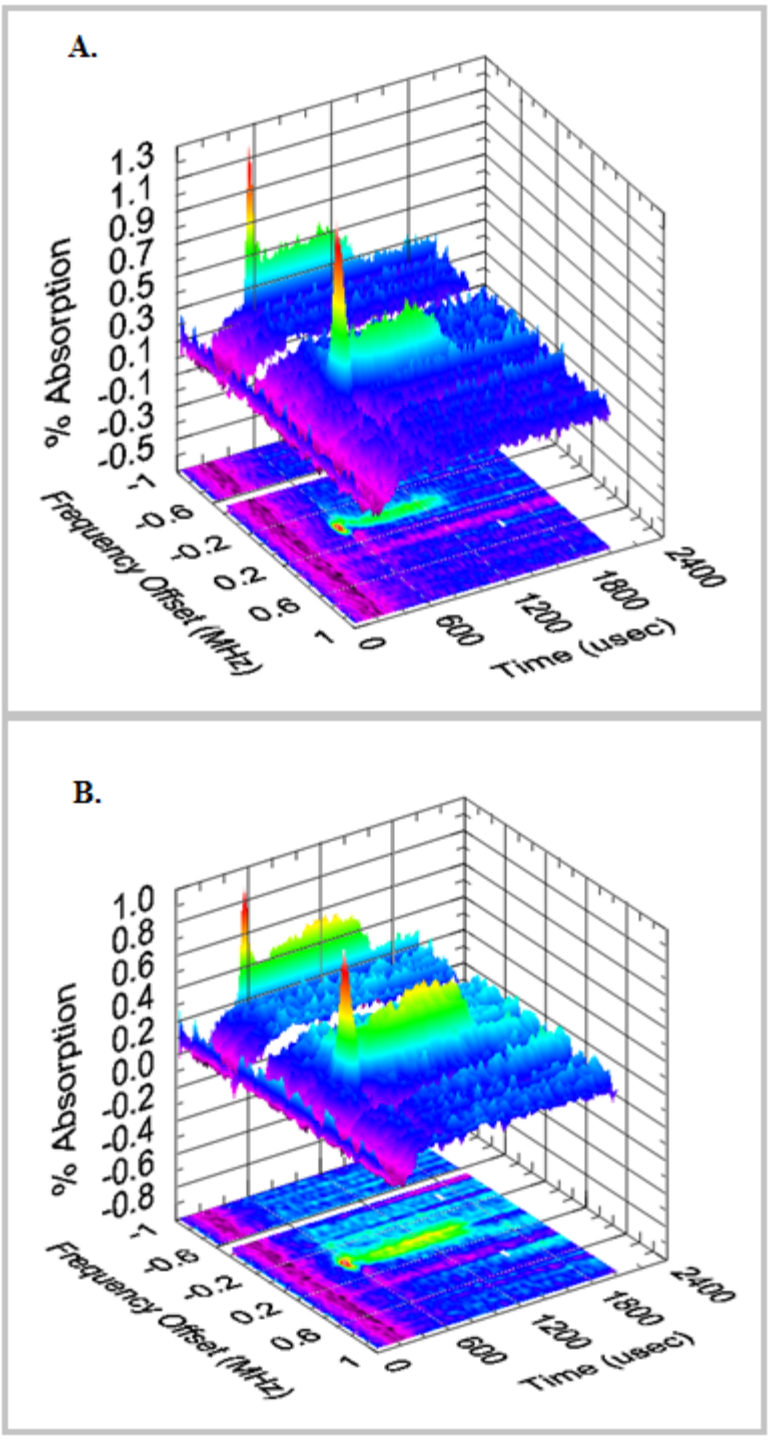

Figure 43. Pinhole expansion scans of ozone J = $2_{11} \leftarrow 2_{20}$ with background subtracted. Center frequency is 96228.3400 MHz. A. 550 μsec pulse length. B. 650 μsec pulse length.

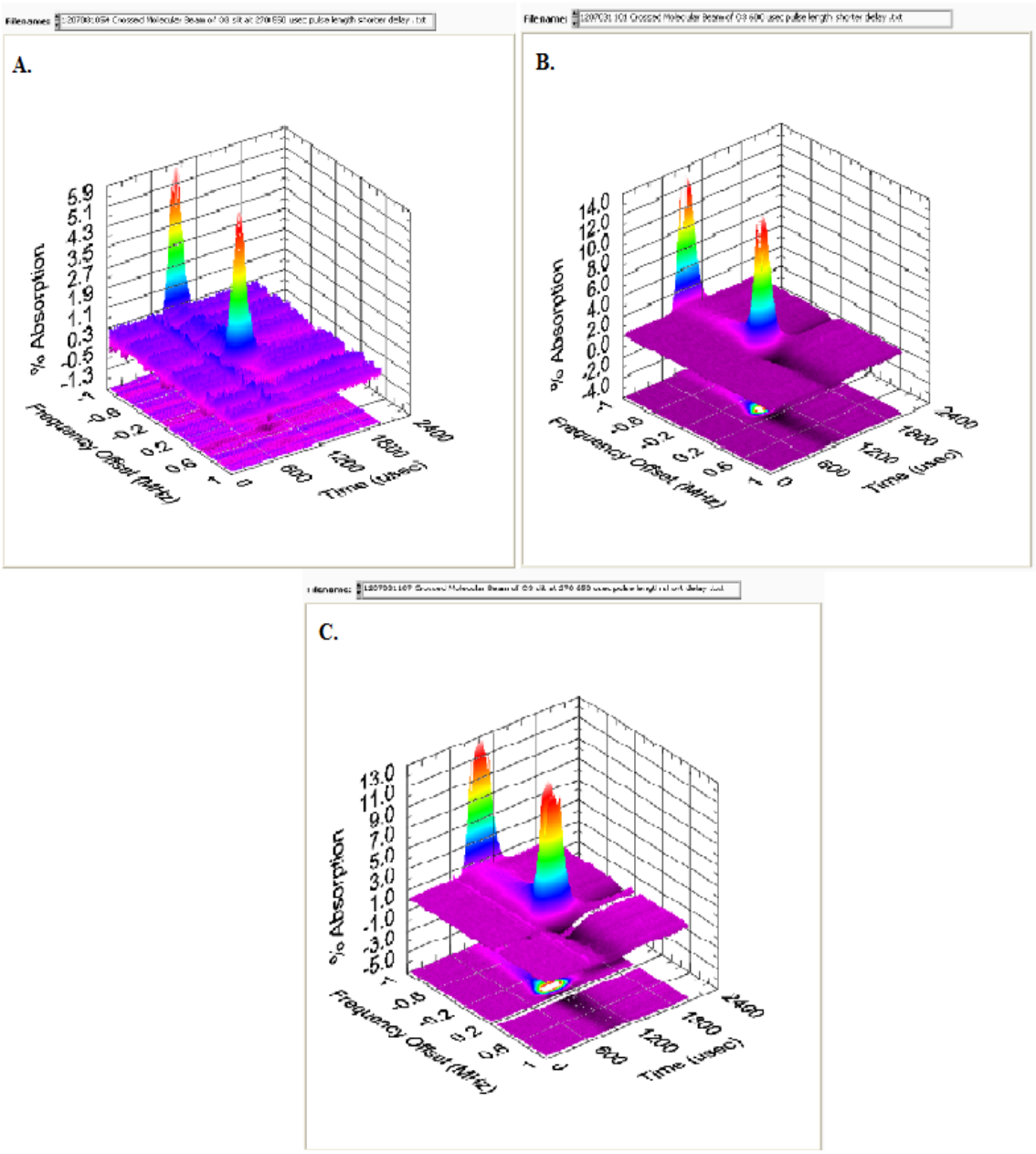

Figure 44. Slit expansion scans of ozone J = $2_{11} \leftarrow 2_{20}$ with background subtracted. Center frequency is 96228.3400 MHz. A. 550 µsec pulse length. B. 600 µsec pulse length. C. 650 µsec pulse length.

III.A.4 ClO Spectrum

Past work in Dr. Duffy's lab resulted in the determination of the rotational transition frequencies of vibrationally excited ClO products, as well as predictions about the transitions not directly observed made by Dr. Edward Cohen at NASA's Jet Propulsion Laboratory [30, 43]. Figure 45 simulates part of the ro-vibrational spectrum for ClO.

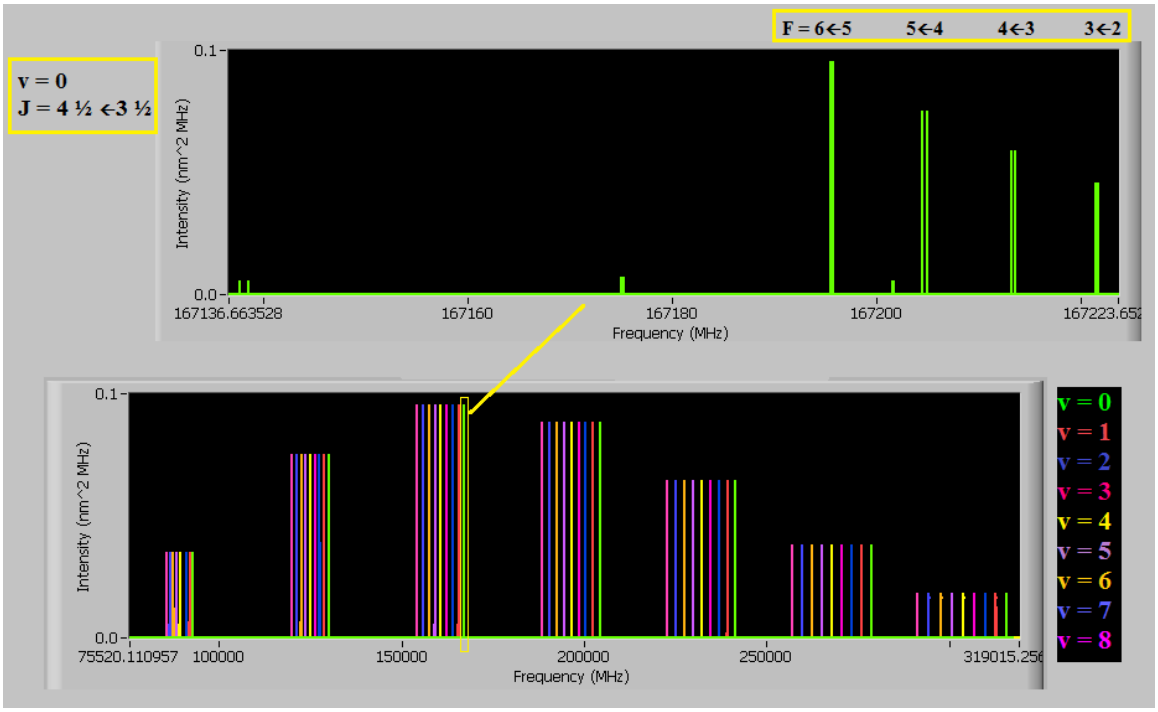

Figure 45. ClO Spectrum. Bottom: Ro-vibrational spectrum for ClO, different values for the vibrational states, v, are color coded. Top: Close up view of the hyperfine structure of the v = 0 rotational lines.

In this ClO spectrum, the color of the peak corresponds to a specific vibrational state and the size of the peak correlates to the relative population of molecules at 13 K. Although they look like single peaks, a close up view reveals that each ro-vibrational peak is

composed of multiple peaks, which are the various possible hyperfine states within. Each one of these hyperfine states consists of a pair of peaks due to the lambda doublet splitting caused by the lifting of the degeneracy of the electronic levels due to tumbling of the molecules. An OClO photodissociation experiment conducted previously in the Duffy lab revealed the vibrational distribution of ClO product molecules, as seen in Figure 46 [43]. In this distribution the same hyperfine rotational state, J = 7 ½, ground Ω = 3/2 spin-orbit state was probed for the different vibrational states. The distribution shows a maximum in the v = 5 state, and while the v = 0 state is also fairly high; it may be partially a result of collisions within the molecular beam causing a relaxation of the vibrationally excited products.

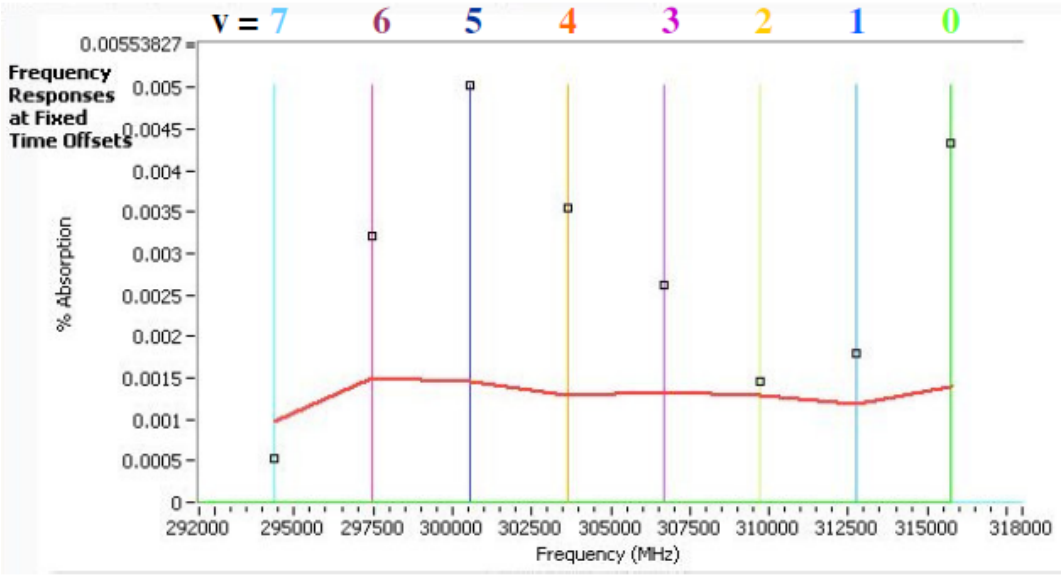

Figure 46. Vibrational distribution of ClO (J = 7 ½, Ω = 3/2) from the photodissociation of OClO at 328 nm. The v = 0 feature gets larger at longer times due to collisions within the molecular beam. The boxes represent the line intensities, while the red line gives the rms noise level [43].

Using this prior knowledge the goal of the crossed molecular beam experiment was to acquire Doppler profiles of ClO products. These scans would have been done on an individual transition and by keeping the arms at a fixed angle and rotating them relative to the source. The profiles could then be used to create a three-dimensional velocity distribution using a mathematical technique called Fourier Transform Doppler Spectroscopy [44]. Scans could have been done for different vibrational states, while keeping the same hyperfine rotational state fixed to get a vibrational distribution similar to the photodissociation one. Finally, the angle of collision could be changed to alter the relative kinetic energy between the reactants. In doing this, the population distributions for vibrational states could be studied based on the angle of collision.

III.B Conclusion

A new crossed molecular beam apparatus was successfully constructed for use in the study of numerous elastic and reactive scattering experiments. The design included a differentially pumped rotating arm system to facilitate colliding reactants at various angles. A new gas inlet system, including a way to recycle reactant species, was built to accommodate the use of multiple nozzles and a new detector design was implemented as a more economical means to run the experiments.

Ozone was successfully and safely produced and trapped, which allowed for the ability to run multiple scans without the degradation of one of the reactant molecules before reaching the reaction chamber. Future possibilities for the ozone system could be to implement a temperature controlled trap bath to keep the concentration of ozone even

more consistent, as well as implementing the inclusion of a UV-Vis spectrophotometer to measure the concentration of ozone at 280 nm.

The discharge system went through several modifications from a pulsed sequence to constant current; however attempts to destroy ozone as a prior test to using chlorine have been unsuccessful. To remedy this situation, a new power supply with a higher output current may be needed and/or a new high voltage high current fast switches need to be purchased. Otherwise a different method such as thermal decomposition method could be implemented, which would still allow for the arms to be rotated freely. The use of methods such as laser dissociation would likely require an arm to remain at a fixed angle, which would not be ideal.

Once a successful Cl atomic beam has been created and a successful $Cl + O_3$ reaction has occurred to produce ClO products, the system can be optimized. This would involve the addition of skimmers and choppers to create a narrow packet of reactant molecules. By creating a small packet of reactants, in frequency and time, the possibility of gas collisions after the reaction can be eliminated to truly probe nascent product distributions. These distributions can then be used to create differential scattering cross sections, which can be used as empirical evidence for theoretical predictions about the nature of the electronic states involved in crossed molecular beam reactions.

REFERENCES

1. Lee, Y. T. Molecular Beam Studies of Elementary Chemical Processes. Nobel Lecture, 8 December **1986**.

2. Herschbach, D. R. Molecular Dynamics of Elementary Chemical Reactions. Nobel Lecture, 8 December **1986**.

3. Scoles, G.; Bassi, D.; Buck, U.; Laine, D., Editors. Atomic and Molecular Beam Methods, Vol. 1. *Oxford University Press*, New York, **1988**.

4. van de Meerakker, S. Y. T.; Bethlem, H. L.; Meijer, G. Taming Molecular Beams. *Nat. Phys.* **2008,** 4 , 595 – 602.

5. Suits, A. G.; Lee, Y. T. "Reactive Scattering." Springer Handbook of Atomic, Molecular, and Optical Physics, *Springer-Verlag*, New York, **2006,** 967 – 982.

6. Levine, R. D. Molecular Reaction Dynamics. *Cambridge University Press*, New York, **2005**.

7. Campargue, R., editor, Atomic and Molecular Beam: The state of the art 2000. *Springer-Verlag*, New York, **2001**.

8. Pauly, H.; Toennies, J. P. The Study of Intermolecular Potentials with Molecular Beams at Thermal Energies. *Advances in Atomic and Molecular Physics* **2006**, Vol. 1, 195 – 344.

9. Zhang, J.; Lee, Y. T. Crossed Molecular Beam Study of the Reaction Cl + O_3. *J. Phys. Chem. A* **1997**, 101, 6485-6495.

10. Molina, L. T.; Molina, M. J. Production of chlorine oxide (Cl2O2) from the self-reaction of the chlorine oxide (ClO) radical. *J. Phys. Chem. A* **1987**, 91, 433-436.

11. McElroy, M. B.; Salawitch, R. J.; Wofsy, S. C.; Logan, J. A. Reductions of Antarctic ozone due to synergistic interactions of chlorine and bromine. *Nature* **1986**, 321, 759-762.

12. Clyne, M. A. A.; Nip, W. S. Study of elementary reactions by atomic resonance absorption with a nonreversed source. Part 1. The reaction of chlorine atoms with ozone giving chlorine monoxide and oxygen. *J. Chem. Soc., Faraday Trans.* **1976**, *2*, 72, 838.

13. Zahniser, M. S.; Kaufman, F.; Anderson, J. G. Kinetics of the reaction atomic chlorine + ozone .far. chlorine oxide (ClO) + molecular oxygen. *Chem. Phys. Lett.* **1976**, *37*, 226.

14. Toohey, D. W.; Brune, W. H.; Anderson, J. G. Rate constant for the reaction Br + O3 → BrO + O2 from 248 to 418 K: kinetics and mechanism. *Int. J. Chem. Kinet.* **1988**, *20*, 131.

15. Nicovich, J. M.; Kreutter, K. D.; Wine, P. H. Kinetics of the reactions of atomic chlorine [Cl(2PJ)] and atomic bromine [Br(2P3/2)] with ozone. *Int. J. Chem. Kinet.* **1990**, *22*, 399.

16. Patrick, R.; Golden, D. M. Kinetics of the reactions of amidogen radicals with ozone and molecular oxygen. *J. Phys. Chem.* **1984**, *88*, 491.

17. Baulch, D. L.; Cox, R. A.; Hampson, R. F. Jr; Kerr, J. A.; Troe, J.; Watson, R. T. Evaluated kinetic and photochemical data for atmospheric chemistry. *J. Phys. Chem. Ref. Data* **1980**, *9*, 295.

18. Baulch, D. L.;Cox, R. A.; Crutzen, P. J.; Hampson, R. F. Jr.; Kerr, J. A.; Troe, J.; Watson, R. T. Evaluated kinetic and photochemical data for atmospheric chemistry: supplement I. CODATA task group on chemical kinetics. *J. Phys. Chem. Ref. Data* **1982**, *11*, 327.

19. Baumgartel, S.; Delmdahl, R.F.; Gericke, K.H.; Tribukait, A.; Reaction dynamics of $Cl+O_3$ -> $ClO+O_2$. *European Physical Journal D* **1998**, *4*, 199-205.

20. Matsumi, Y.; Nomura, S.; Kawasaki, M.; Imamura, T.; Vibrational distribution of ClO radicals produced in the reaction $Cl+O_3$->$ClO+O_3$. *Journal of Physical Chemistry* **1996**, *100*, 176-179.

21. Tyrrell, J.; Kar, T.; Bartolotti, L.J.; A study of the mechanism of the reaction between ozone and the chlorine atom using density functional theory. *Journal of Physical Chemistry A* **2001**, *105*, 4065-4070.

22. Hwang, D.Y.; Mebel, A.M.; Ab initio study on the reaction mechanism of ozone with the chlorine atom. *Journal of Chemical Physics* **1998**, *109*, 10847-10852.

23. Carter, R.O.; Andrews, L.; Matrix Spectroscopic Studies of Chlorine Atom-Ozone Reaction-Products. *Journal of Physical Chemistry* **1998**, *85*, 2351-2354.

24. Baumgartel, S.; Gericke, K.H.; Nascent State-Resolved ClO in Reactions and Photodissociation Processes. *Chemical Physics Letters* **1998**, *227*, 461-466.

25. Murrell, J.N.; Sorbie, K.S.; Varandas, A.J.C.; Analytical Potentials for Triatomic Molecules from Spectroscopic Data .2. Application to Ozone. *Molecular Physics* **1976**, *32*, 1359-1372.

26. Rathmann, T.; Schindler, R. N. Ab initio calculations on the geometries and thermodynamic stabilities of chlorine trioxides. *Chem. Phys. Lett.* **1992**, *190*, 539.

27. Rathmann, T.; Schindler, R. N. Ab initio calculations on selected chlorine oxygen compounds. *Ber. Bunsen-Ges. Phys. Chem.* **1992**, *96*, 421.

28. Vanderzanden, J. W.; Birks, J. W. Formation of oxygen atoms in the reaction of chlorine atoms with ozone. *Chem. Phys. Lett.* **1982**, *88*, 109.

29. Choo, K. Y.; Leu, M. Determination of molecular oxygen(1.sum.g+) and molecular oxygen(1Δg) yields in atomic chlorine + molecular oxygen and atomic chlorine + ozone reactions. *J. Phys. Chem.* **1985**, *89*, 4832.

30. Duffy, L. M. Photodissociation dynamics in “hyper-rovibronic” detail: Exploring the potential of millimeter/submillimeter-wave spectroscopy in molecular reaction dynamics experiments. *Rev. Sci. Instrum.* **2005**, *76*, 093104 – 093111.

31. Christen,W. & Rademann, K. Cooling and slowing in high-pressure jet expansions. *Phys. Rev. A* **2008**, *77*, 012702.

32. Cook, G. A.; Kiffer, A. D.; Klumpp, C. V.; Malik, A. H.; Spence, L. A. Separation of ozone from oxygen by a sorption process. *Adv. Chem. Ser.* **1959**, *21*, 44.

33. Clough, P. N.; Thrush, B. A. A safe method of preparing concentrated ozone. *Chem. Ind.* **1966**, *19*, 1971.

34. Atyaksheva, L. F.; Emel'yanova, G. I. Russ. Physical-chemical processes in the sorption of dilute ozone and oxygen. *J. Phys. Chem*. **1990**, *64*, 1741.

35. Brouard, M.; Duxon, S.; Enriquez, P. A.; Simons, J. P.; Chem, J. The stereodynamics of photon induced reactions via Doppler resolved LIF spectroscopy: photodissociation dynamics of $HONO_2$ and the reaction dynamics of $O(^1D)$ with CH_4. *Soc. Faraday Trans*. **1993**, *89*, 1435.

36. Sibener, S. J.; Buss, R. J.; Cassavechia, P.; Hirooka, T.; Lee, Y. T. A crossed molecular beam study of the atomic oxygen (1D2) + methane reaction. *J. Chem. Phys*. **1980**, *73*, 6351.

37. Continetti, R. E.; Balko, B. A.; Lee, Y. T. Crossed molecular beams study of the reaction $D+H_2 \rightarrow DH+H$ at collision energies of 0.53 and 1.01 eV. *J. Chem. Phys*. **1990**, *93*, 5719.

38. Ren, Z., Qiu, M., Che, L., Dai, D., Wang, X., and Yang, X. A double-stage pulsed discharge fluorine atom beam source. *Review of Scientific Instruments* **2006**, *77*, 016102.

39. Goldsmith, P. F. Quasi-Optical Techniques. *Proc. IEEE*. **1992**, *80(11)*, 1729-1742.

40. Demtröder. Laser Spectroscopy: Basic Concepts and Instrumentation, New York: Springer-Verlag, **1996**.

41. NASA Jet Propulsion Laboratory, "Molecular Spectroscopy," [Online]. Available: http://spec.jpl.nasa.gov/. [Accessed June 2012].

42. Townes, C. H.; Schawlow, A. L.; Microwave Spectroscopy. *Dover Publications Inc*., New York, **1975**.

43. Layne, B. H.; Duffy, L. M. Photodissociation of OClO detected by a 'virtual bolometer': the development of the BASIS technique and the latest on the detection of ClO vibrational product distributions in hyper ro-vibronic detail. Poster session presented at the *29th International Symposium on Free Radicals* August **2007**, Big Sky, Montana, USA.

44. Kinsey, J. L. Fourier Transform Doppler Spectroscopy: A new means of obtaining velocity-angle distributions in scattering experiments. *J. Chem. Phys*. **2006**, *66*, 2560 – 2565.

45. P. Atkins and J. de Paula. Physical Chemistry 8th Edition, New York: W.H. Freeman and Company, **2006**.

46. P. L. Houston. Chemical Kinetics and Reaction Dynamics, Mineola, N.Y.: Dover Publications Inc., **2001**.

47. Scoles, G.; Laine, D.; Valbusa, U., Editors. Atomic and Molecular Beam Methods, Vol. 2. *Oxford University Press*, New York, **1988**.

48. Moore, J. H.; Davis, C. C.; Coplan, M. A. Building Scientific Apparatus 4th Edition. *Cambridge University Press*, New York, **2009**.

49. Gordy, W.; Smith, W. V.; Trambarulo, R. F.; Microwave Spectroscopy. *Dover Publications Inc*., New York, **1953**.

50. Kroto, H. W. Molecular Rotation Spectra. *Dover Publications Inc*., New York, **1992**.

51. Electronic components were made and/or modified by Michael Shelton and Charlie Shepherd in the instrument support facility at UNCG.